OPEN REPORT
SCK•CEN-BLG-1077

Interatomic Potential to Simulate Radiation Damage in Fe-Cr Alloys

Development and Validation

G. Bonny, R.C. Pasianot, D. Terentyev and L. Malerba

March, 2011

SCK•CEN
Boeretang 200
2400 Mol
Belgium

Nuclear Materials Science Institute
Structural Materials Group

OPEN REPORT OF THE BELGIAN NUCLEAR RESEARCH CENTRE
SCK•CEN-BLG-1077

Interatomic Potential to Simulate Radiation Damage in Fe-Cr Alloys

Development and Validation

G. Bonny, R.C. Pasianot, D. Terentyev and L. Malerba

March, 2011
Status: Unclassified
ISSN 1379-2407

SCK•CEN
Boeretang 200
2400 Mol
Belgium

Nuclear Materials Science
Institute
Structural Materials Group

© SCK•CEN
Belgian Nuclear Research Centre
Boeretang 200
2400 Mol
Belgium

Phone +32 14 33 21 11
Fax +32 14 31 50 21

http://www.sckcen.be

Contact:
Knowledge Centre
library@sckcen.be

Executive Summary

The commonly proposed structural materials for advanced nuclear reactors are high-Cr ferritic-martensitic steels (~9-12 at.% Cr), possibly containing oxide particles. This choice is supported by their superior thermal, corrosion and radiation resistance as compared to austenitic steels. A first approximation to describe such steels in a modelling framework is the Fe-Cr binary model alloy.

Density functional theory (DFT) calculations show that the mixing enthalpy of the Fe-Cr binary changes sign with Cr content. It is negative below a critical concentration ~10 at.% Cr and positive above it. A negative mixing enthalpy indicates solubility and a tendency to partial ordering, while a positive value indicates the clustering of Cr into a separate Cr-rich phase (α' phase).

In the literature it has been shown that such a complex thermodynamic behaviour cannot be reproduced in terms of atomic interactions within a simple and widely used embedded atom method (EAM) framework. Therefore, two extensions of the EAM have been proposed, namely, the two-band model (2BM) and the concentration dependent method (CDM), both introducing a local concentration variable in the EAM. For each formalism, a potential describing the Fe-Cr alloy is available in the literature that reproduces the change of sign in the mixing enthalpy, however suffer of some important shortcomings.

A first shortcoming concerns the pure elements, which in both cases are described by the same potentials. In particular, the pure Fe potential does not provide stable glide of the ½ ⟨111⟩ screw-dislocation in the (110) plane, in contrast with experiments. The pure Cr potential, on the other hand, does not predict a compact core of the ½ ⟨111⟩ screw-dislocation, in contrast with DFT data. To overcome both shortcomings, different but otherwise equally performing potentials were selected and fitted for pure Fe and Cr, respectively.

Regarding the alloy, the potential fitted in the 2BM formalism predicts stable intermetallic compounds at the Cr-rich side, which are experimentally not observed and contradict DFT calculations. As a consequence, the mixing enthalpy is negative in the same region, again contradicting DFT calculations. The potential fitted in the CDM formalism, on the other hand, largely underestimates the experimentally observed excess vibrational entropy. As a result, the phase diagram corresponding to that potential fails to describe full solubility below melting temperature, in disagreement with the experimental phase diagram where full solubility is observed above 900 K. In addition, interstitial defects in bulk Fe containing Cr are poorly described, as are the vacancy migration barriers. To overcome the shortcomings of both potentials, we develop a new one within a generalized 2BM model.

The performance of the different potentials, including our own, is briefly sketched in the table below.

Potential	Thermodynamics			Point-Defects			Dislocations
	Disordered Alloy	Intermetallic Compounds	Vibrational Entropy	Substitutional	Interstitial	Migration	
Here	Consistent	Consistent	Underestimated	Consistent	Consistent	Consistent	Consistent
2BM	Inconsistent	Inconsistent	Overestimated	Consistent	Consistent	Consistent	Inconsistent
CDM	Consistent	Consistent	Inconsistent	Consistent	Inconsistent	Inconsistent	Inconsistent

This report contains a detailed description regarding the development of the Fe-Cr potential within the GetMat and EFDA project.

Relevant Publications:

- G. Bonny, R.C. Pasianot, D. Terentyev, L. Malerba, "Iron chromium potential to model high-chromium ferritic steels", *Philosophical Magazine* 91 (2011) 1724.
- G. Bonny, R.C. Pasianot, E.E. Zhurkin, M. Hou, "Determination of the phase diagram from interatomic potentials: The iron-chromium case", *Computational Materials Science* (2011), in press, doi: 10.1016/j.commatsci.2011.02.032.
- D. Terentyev, G. Bonny, N. Castin, C. Domain, L. Malerba, P. Olsson, V. Moloddtsov, R.C. Pasianot, "Further development of large-scale atomistic modelling techniques for Fe-Cr alloys: Current status", *Journal of Nuclear Materials* 409 (2011) 167.
- T.P.C. Klaver, G. Bonny, P. Olsson and D. Terentyev, "Benchmarking FeCr empirical potentials against Density Functional Theory data", *Modelling and Simulation in Materials Science and Engineering* 18 (2010) 075004.
- D. Terentyev, G. Bonny, C. Domain and R.C. Pasianot, "Interaction of a ½<111> screw dislocation with Cr precipitates in bcc Fe studied by molecular dynamics", *Physical Review B* 81 (2010) 214106.
- G. Bonny, R.C. Pasianot, L. Malerba, "Interatomic potentials for alloys: Fitting concentration dependent properties", *Philosophical Magazine* 89 (2009) 711.

Table of Contents

1. Introduction 4
2. State-of-the-Art and Objectives 4
3. Definitions and Methods 5
3.1. Definitions 5
3.2. Methods 6
4. Fitting Methodology 7
4.1. Pure Elements 7
4.2. Alloy 9
5. Validation of the Potential 11
5.1. Pure Elements 11
5.2. Thermodynamic Properties of the Alloy 13
5.2.1. Mixing Enthalpy of Disordered Alloys 14
5.2.2. Formation Energy of Intermetallic Compounds 14
5.2.3. Excess Vibrational Entropy 15
5.2.4. Phase Diagram 16
5.3. Point-Defect Properties in the Alloy 17
5.3.1. Substitutional Defects 17
5.3.2. Interstitial Defects 19
6. Concluding Remarks 22
Acknowledgements 23
Appendix A: Chromium Potential 24
Appendix B: Iron-Chromium Potential 25
Appendix C: Some Numerical Issues 30
Appendix D: Intermetallic Compounds 31
Appendix E: Vacancy Migration Barriers 32
Appendix F: Binding Energy of Interstitial Configurations 33
References 36

1. Introduction

The commonly proposed structural materials for advanced nuclear reactors are high-Cr ferritic-martensitic steels (~9-12 at.% Cr), possibly containing oxide particles. This choice is supported by their superior thermal, corrosion and radiation resistance as compared to austenitic steels. A first approximation to describe such steels in a modelling framework is the Fe-Cr binary model alloy.

The addition of chromium to iron influences significantly the response of the alloy to irradiation. It has been shown that the swelling in Fe-Cr is about one order of magnitude lower than in pure Fe for the same dose [1-5]. A remarkable effect of Cr is also observed in the shift of the ductile-to-brittle transition temperature (DBTT) in irradiated ferritic-martensitic steels. This shift is found to reach a minimum around 9 at.% Cr [6, 7], in a range of irradiation temperatures from 300 to 410°C and for doses from 7 to 36 dpa. This result is in fact the main reason for choosing Cr concentrations around 9 at.% in most steels proposed for nuclear applications.

Even in the absence of irradiation, the Fe-Cr system exhibits a number of peculiarities. Density functional theory (DFT) calculations on the Fe-Cr binary have shown that the mixing enthalpy exhibits a change of sign [8-14], which is negative below a critical concentration ~10 at.% Cr and positive above it. A negative mixing enthalpy indicates solubility and a tendency to partial ordering, while a positive value indicates that Cr clusters into a separate Cr-rich phase (α' phase). These results are compatible with experimental observations that show an inversion of the sign of the short-range order (SRO) parameter from negative to positive, with the zero crossing occurring at about 10 at.% Cr [15-17]. This behaviour is reflected in the Fe-Cr equilibrium phase diagram [18], which was recently revised [19] and consists of a meta-stable miscibility gap (when ignoring the sigma phase) with large Cr solubility even at low temperature (~8 at.% Cr).

In order to better understand the behaviour of Fe-Cr alloys under irradiation, it is very desirable to gain understanding at the atomic level, large scale molecular dynamics (MD) and Monte Carlo (MC) simulations being the tools of choice. These tools, however, hinge in an essential manner on the interatomic potentials employed, which therefore must strike a balance between the conflicting needs of computational speed and reliability. Thus, an interatomic potential describing the Fe-Cr alloy reasonably well in the temperature range of interest is needed.

2. State-of-the-Art and Objectives

In the literature two interatomic potentials have been developed in an embedded atom method (EAM) like formalism capable of reproducing Fe-Cr's heat of mixing complex behaviour as a function of composition. These are a two-band model (2BM) potential developed by Olsson *et al.* [20] (henceforth OLS) and a concentration dependent model (CDM) potential developed by Caro *et al.* [21] (henceforth CAR). The 2BM is a modification of the EAM, where a second embedding term is added to account for contribution of s-band electrons. The CDM, on the other hand, keeps the EAM form but has a mixed pair interaction that depends on both distance and a local concentration variable. Although formally different, both formalisms have been shown to be equally capable of reproducing any shape of mixing enthalpy [22]. In addition, OLS (strictly, the one fitted to PAW data from [20, 23]) has proven to provide a very reasonable description of the interaction between Cr and point-defects in Fe ([24-26], and references therein).

While using them, however, it has become clear that both potentials suffer from some important drawbacks. A first shortcoming concerns the pure elements, which in both cases are described by the same single-element potentials. In particular, the pure Fe potential developed by Ackland *et al.* [27] (henceforth A04) does not provide stable glide of the ½ ⟨111⟩ screw-dislocation in the (110) plane when subjected to a load. This shortcoming prevents the pinning of the screw dislocation by Cr-rich precipitates, as suggested by experiments. The pure Cr potential developed by Olsson *et al.* [20] (henceforth O05), on the other hand, does not predict a compact core of the ½ ⟨111⟩ screw-dislocation, in contrast with DFT calculations.

Regarding the alloy, OLS predicts stable intermetallic compounds at 50 at.% Cr and at the Cr-rich side (> 90 at.% Cr), which are experimentally not observed and contradict DFT calculations [28]. As a consequence, the mixing enthalpy is negative above 90 at.% Cr, which again contradicts DFT calculations. The CAR potential, on the other hand, largely underestimates the experimentally observed excess vibrational entropy [28, 29]. As a result, the predicted phase diagram fails to describe full solubility below melting temperature, in disagreement with the experimental phase diagram where full solubility is observed above 900 K. In addition, the interaction of Cr atoms with interstitial defects in the Fe matrix is poorly described (as is shown in this report), as are the vacancy migration barriers [26]. We note, however, that the CAR potential was not fitted to the latter properties.

Thus, the objective of this work is to fit a new 2BM potential that overcomes the drawbacks of both existing potentials, without losing their good properties. In this report the newly developed potential is presented, and validated to DFT and experimental data. In addition, all obtained data are compared to data from the OLS and CAR potentials.

3. Definitions and Methods

3.1. Definitions

For localized or periodic defect structures (e.g. points defects and intermetallic compounds, respectively), we define the formation energy, E_f, for a configuration X consisting of N_{Fe} Fe atoms and N_{Cr} Cr atoms as,

$$E_f(X) = (N_{Fe} + N_{Cr})E(X) - N_{Fe}E(\mathrm{Fe}) - N_{Cr}E(\mathrm{Cr}), \quad (1)$$

where E(X), E(Fe) and E(Cr) are the average energy per atom for configurations X, bulk Fe and bulk Cr, respectively. Based on the formation energy of localized defects, we define the binding energy E_b between N such defects $X_1,\ldots,X_N$ as,

$$E_b(X_1,...,X_N) = \sum_{k=1}^{N} E_f(X_k) - E_f(X_1,...,X_N), \quad (2)$$

namely, as the energy needed to break up the complex ($X_1,\ldots,X_N$) into its individual, non-interacting constituents; thus positive/negative values indicate attraction /repulsion.
Also commonly used is the interaction energy, E_I, defined as the opposite of E_b (E_I=-E_b). An often here encountered instance refers to the case of two Cr atoms forming part of a defect complex *(XY)*; we define ([12]) the net interaction, E_I(CrCr), as

$$E_{\mathrm{I}}(\mathrm{CrCr}) = E_{\mathrm{b}}(XY) - E_{\mathrm{b}}(X) - E_{\mathrm{b}}(Y)\,, \tag{3}$$

being X (Y) the defect complex containing the first (second) Cr atom only.

For disordered or short-range ordered alloys, the excess quantity, F_{xc}, of the thermodynamic function, F, is defined as

$$F_{\mathrm{xc}}(x) = F(x) - x_{\mathrm{Fe}}F(\mathrm{Fe}) - x_{\mathrm{Cr}}F(\mathrm{Cr})\,, \tag{4}$$

with x the concentration. When taking the enthalpy per atom and the vibrational entropy per atom as thermodynamic functions, one obtains the mixing enthalpy, E_{mix}, and excess vibrational entropy, $S_{\mathrm{xc}}^{\mathrm{vib}}$, respectively.

3.2. Methods

To compute the formation energy of defect structures, simulation crystals containing 2000 atoms were relaxed using the conjugate gradient method. For localized defects we relaxed the atomic coordinates at constant volume (the equilibrium lattice of the matrix element), while for periodic structures the atomic coordinates, crystal shape and volume were relaxed. The migration energies of point-defects were calculated in similar simulation crystals, at constant volume, using the nudged elastic band method [30]. To mimic disordered alloys, the desired number of solute atoms were distributed at random in the above simulation crystals, and the same relaxation procedure as for periodic structures was applied in order to find the equilibrium configurations. Excess quantities were finally derived from such simulation crystals.

The vibrational entropy per atom, S^{vib}, in the harmonic approximation and high temperature limit is obtained as [31],

$$S^{\mathrm{vib}} = -k_{\mathrm{B}}\sum_{m}\ln\left(\frac{\hbar\omega_m}{k_{\mathrm{B}}T}\right), \tag{5}$$

with k_{B} Boltzmann's constant, T the absolute temperature, $\hbar$ the reduced Planck constant and ω_m the angular frequencies associated with the eigenvalues, ω_m^2, of the force constants matrix, Φ. For a system containing N atoms, the latter contains $3N\times3N$ elements (3 Cartesian components per atom) and is given as,

$$\Phi_{ij}^{\alpha\beta} = \frac{1}{\sqrt{m_i m_j}}\frac{\partial^2 E}{\partial r_i^{\alpha}{}_i \partial r_j^{\beta}}\,. \tag{6}$$

with m_i and r_i the mass and coordinate associated with atom i, respectively.

The phase diagram corresponding to our potential was calculated using the (freely available) ATAT package [32, 33], which has been interfaced to an in-house MD code working as "energy engine". Broadly, the package works in two stages: firstly, an automated statistically optimised procedure is followed in order to build a cluster expansion of the energy on the bcc lattice (this is where the MD code, namely the interatomic potential, enters); secondly, the previous expansion is fed to a Monte Carlo code working in the

transmutation (semi-grand canonical) ensemble for tracking the phase boundaries. The cluster expansion is here used as an economic way to compute the energy of any configuration of the simulation crystal. The transmutation ensemble allows the species to change their nature, so that the controlling variables are T and chemical potentials difference, μ. Also, the simulation crystals referred to above are not strictly rigid, because atomic relaxations are accounted for when building the cluster expansion. The method takes the configurational entropy implicitly into account. Vibrational entropy, as obtained from Equation (5), is accounted for by temperature dependent cluster coefficients, as discussed in [28, 34].

4. Fitting Methodology

4.1. Pure Elements

For the pure elements (Fe and Cr), the atomic interactions are described using the embedded atom method (EAM) [35], which is widely used to describe metals. For both elements, a range of EAM-type interatomic potentials are available. For our purpose the one developed by Mendelev *et al.* [36] seems to be the most suited (see Section 5.1) to describe Fe, while for Cr, we opted to fit a new potential (see Section 5.1) following the scheme described below.

Within the EAM scheme, in addition to accounting for pair interactions, V, the expression for the total energy of the system includes an embedding energy, F, dependent on the (heuristically) local electron density, ρ. The latter contribution approximates the many-body effect of all nearby atoms. The total energy within the EAM is accordingly given as,

$$E = \frac{1}{2}\sum_{i,j(i\neq j)} V(r_{ij}) + \sum_{i} F(\rho_i), \tag{7}$$

where the indices i and j run over all atoms in the system and r_{ij} is the distance between atoms i and j. The local electron density around atom i, contributed from its neighbours is given as,

$$\rho_i = \sum_{j(j\neq i)} \varphi(r_{ij}), \tag{8}$$

where φ denotes the electron density function. It must be noted, however, that there exist two transformations, $\hat{T}_1$ and $\hat{T}_2$, that leave the total energy invariant [37-39],

$$\hat{T}_1 \begin{cases} \varphi(r) \rightarrow S\varphi(r) \\ F(\rho) \rightarrow F(\rho/S) \end{cases}, \tag{9}$$

$$\hat{T}_2 \begin{cases} F(\rho) \rightarrow F(\rho) + C\rho \\ V(r) \rightarrow V(r) - 2C\varphi(r) \end{cases}, \tag{10}$$

with C and S arbitrary constants. Therefore V, ρ and F are not uniquely determined and lose their (originally pretended) physical meaning. A convenient choice for the gauge constants is C=-$F'(\rho_{eq})$ and S=1/ρ_{eq} on the equilibrium lattice. This choice corresponds to the "effective gauge" form [37], where $F'(\rho_{eq})$=0 and ρ_{eq} =1 on the equilibrium lattice. In this representation,

the pair potential gives the effective interaction between two atoms while accounting for first order many-body effects.

Prior to fitting the pair interaction V and the embedding term F, we have to define a reasonable form for the electron density function φ. For this purpose, in this work, we selected a simple Thomas-Fermi screening function which is shifted and truncated for a smooth cut-off between third and fourth nearest neighbour distance (on the bcc equilibrium lattice),

$$\varphi(x) = \varphi_0 \left(\frac{\exp(-\beta x}{x} - \frac{\exp(-\beta x_{\text{cut}})}{x_{\text{cut}}} \right) f_{\text{cut}}(x) , \tag{11}$$

with $x = r / r_0^{1\text{nn}}$, r the distance in Å, r_0^{1nn} the nearest neighbour distance on the bcc equilibrium crystal with lattice parameter a_0=2.878Å, $x_{\text{cut}} = 1.65\, r_0^{1\text{nn}}$ the cut-off distance, φ_0=0.0676504617 a constant normalization factor and β=5. The cut-off function f_{cut} is defined as,

$$f_{\text{cut}}(x) = \begin{cases} 1 & , \quad x \le 1 \\ 1 - \dfrac{(x-1)^3}{(x_{\text{cut}}-1)^3} & , \quad 1 < x \le x_{\text{cut}} \\ 0 & , \quad x_{\text{cut}} < x \end{cases} . \tag{12}$$

The pair interaction V is parameterized by the cubic spline expansion,

$$V(r) = \sum_{k=1}^{N} a_k \, (r_k - r)^3 \Theta(r_k - r) , \tag{13}$$

where N denotes the number of knots, a_k are the fitting parameters and Θ the Heaviside unit step function. As explained below, the embedding term F is only available in numerical format.

Generally, the fitting of an interatomic potential to material properties is a problem of matching data obtained from a trial potential function to a given data set. This problem can be cast into one of minimizing the overall squared deviation, so-called objective function (OF), between the calculated properties and the associated reference data, possibly also imposing certain constraints. In a first approximation, we neglect relaxation effects, so that a local optimizer is sufficient. In our case (see Equation (13)), such a scheme reduces to a quadratic programming problem [40] that can be solved exactly.

The essential material properties considered in the fit are the correct lattice stability, the cohesive energy E_{coh}, the equilibrium lattice constant a_0, the elastic constants (for cubic lattice structures) C_{11}, C_{12}, C_{44} [41], and the vacancy formation energy, E_{f}^{V}. In addition to these, we also included in the fit the formation energy of self-interstitial configurations (dumbbells along the ⟨100⟩, ⟨110⟩ and ⟨111⟩ directions), the vacancy migration energy, E_{m}^{V}, the (110) ⟨111⟩ gamma surface cut, γ, and the ½ ⟨111⟩ screw-dislocation core structure. In particular, the gamma surface cut (~10 points) was fitted through the OF, only using the effective pair potential (i.e. neglecting higher order many-body contributions). The lattice parameter (zero

pressure), unrelaxed vacancy formation energy, E_f^V, and the three elastic constants were fitted through equality constraints. The bcc lattice stability against fcc and the Duesbery & Vitek condition for a compact ½ ⟨111⟩ screw dislocation core ($\gamma(b/3)$ - 2 $\gamma(b/6) > 0$ [42], with b the length of the burgers vector) were fitted through inequality constraints.

Given the effective pair potential, the embedding function is computed by subtraction from Rose's equation [43], which describes the energy per atom $E(\tilde{a})$ for the lattice under uniform expansion or contraction. The expression as a function of the nearest neighbour distance, r^{1nn}, is given as,

$$E(\tilde{a}) = -E_{coh}(1+\tilde{a})\exp(-\tilde{a}). \tag{14}$$

Here $a = \alpha(r_{1nn}/r_0^{1nn} - 1)$ and $\alpha^2 = 9\Omega B / E_{coh}$, where Ω is the atomic volume and B is the bulk modulus. This embedding function, however, is not the one entering the potential. In order to assure a smooth behaviour and particularly constrain the function curvature to remain positive throughout and decreasing at high density, the former embedding is re-fitted on a discrete number of points (~100) taken as reference data. The fit is performed in a minimum square sense and by a cubic spline expansion (also fulfilling $F'(0)=0$). It is the latter expansion that constitutes the embedding function. The price paid for a smooth behaviour is a violation of Rose's equation; however, this can hardly matter, because in the applications of interest the lattice will never be subjected to the kind of uniform, large, contractions and dilations that are probed by Rose's equation.

To conclude, we mention that the full potential was manually (i.e. by trial and error) adjusted in the small distance region to fit the DFT obtained values for interstitial formation energies. The potential's parameters from this procedure are presented in Appendix A.

4.2. Alloy

Although both pure elements are described in the EAM formalism, the latter cannot reproduce complex shapes of the mixing enthalpy [22], as is the case for Fe-Cr, and needs to be extended. In this work we choose the 2BM formalism [20] to describe the Fe-Cr system. Within this formalism the total energy is given as in the EAM with an extra embedding term, F^s,

$$E = \frac{1}{2}\sum_{i,j(i\neq j)} V_{t_i t_j}(r_{ij}) + \sum_i F_{t_i}^d(\rho_i^d) + \sum_i F_{t_i}^s(\rho_i^s), \tag{15}$$

that stems from the s-band electrons, while the standard embedding, F^d, is thought of as resulting from the d-band; t_i denotes the atom type (in our case Fe or Cr) on site i. The electron densities, ρ^d and ρ^s, for the d- and s-band, respectively, are calculated as,

$$\rho_i^\lambda = \sum_{j(j\neq i)} \varphi_{t_i t_j}^\lambda(r_{ij}). \tag{16}$$

Here φ^d and φ^s are the d- and s-density functions, respectively, which comply to the relations,

$$\begin{cases} \varphi^{\mathrm{d}}_{AA} = \varphi^{\mathrm{d}}_{BA} = \varphi^{\mathrm{d}}_{A} \\ \varphi^{\mathrm{d}}_{BB} = \varphi^{\mathrm{d}}_{AB} = \varphi^{\mathrm{d}}_{B} \\ \varphi^{\mathrm{s}}_{AA} = \varphi^{\mathrm{s}}_{BB} = 0 \\ \varphi^{\mathrm{s}}_{AB} = \varphi^{\mathrm{s}}_{BA} \end{cases} . \tag{17}$$

With this choice, the d-density reduces to the EAM density, and the s-density samples the local concentration [22]. In this way the s-embedding terms are only relevant to the alloy, and do not contribute to the pure elements' energy, which keeps the standard EAM expression.

As mentioned in Section 4.1, for the pure elements the units of the electron density are arbitrary. From Equations (16) it is clear, however, that the d-density functions of both elements contribute to the total d-density and therefore to each others d-embedding energy. To assure *a priori* an equal contribution to the d-electron density from all elements, we use transformations $\hat{T}_1$ and $\hat{T}_2$ (see Section 4.1) to transform the potentials for both pure elements in their effective gauge form, prior to fitting the alloy.

Given the EAM potentials for the pure elements and prior to fitting V_{Fe}, V_{Cr}, $F^{\mathrm{s}}_{\mathrm{Fe}}$ and $F^{\mathrm{s}}_{\mathrm{Fe}}$ we define a reasonable form for the electron density function φ^{s}. In line with [20], the square of a 4s-type Slater function is chosen,

$$\varphi^{\mathrm{s}}_{\mathrm{FeCr}} = K\, r^6 \exp(-2\zeta r)\, g_{\mathrm{cut}}(r) . \tag{18}$$

Here K=20.34075425 is a normalisation constant, ζ=2.5001 and g_{cut} is a cut-off function to provide a smooth cut-off between fifth and sixth nearest neighbour distance,

$$g_{\mathrm{cut}}(r) = \begin{cases} 1 & , \quad r \le r_c^i \\ \frac{1}{2}\left[1 - \sin\left(\frac{\pi}{2}\frac{(r - r_m)}{d}\right)\right] & , \; r_c^i < r \le r_c^f \\ 0 & , \; r_c^f < r \end{cases} , \tag{19}$$

with r_c^i=5.1Å the inner cut-off, r_c^f=5.3Å the outer cut-off, $r_m = (r_c^i + r_c^f)/2$ and $d = (r_c^f - r_c^i)/2$. The mixed pair interaction V_{FeCr} is parameterized by a cubic spline expansion given by Equation (13) while the s-embedding functions F^{s} are parameterized by an extended second moment expression similar to [20, 44],

$$F^{\mathrm{s}}(\rho) = A_1 \sqrt{\rho} + A_2\, \rho^2 , \tag{20}$$

with A_1 and A_2 fitting parameters. In principle, a spline expansion as in [22] is an equally good choice for the purpose of fitting the mixing enthalpy, but the square root proved to be essential in reproducing the correct trends in Cr-Cr and Cr-vacancy interaction. Note that transformations $\hat{T}_1$ and $\hat{T}_2$ (see Section 4.1) apply to the s-density function φ^{s}, the s-embedding functions F^{s} and the mixed pair potential V_{FeCr}, as well. They too are therefore not uniquely defined (see [22] for more details). In this work we normalized the (maximum) s-density such that unity corresponds to a single Cr hosted in the Fe matrix.

The mixed pair interaction, as well as both s-embedding functions, were fitted simultaneously to all properties of interest, on a rigid lattice through an OF, similarly to Section 4.1. In this scheme, the optimization problem is again reduced to a quadratic programming problem that can be solved exactly. The mixing enthalpy was fitted in the whole concentration range (~50 points) using a variance expansion as described in [22], while at each concentration a zero pressure condition was imposed to obtain a lattice parameter as close as possible to the linear interpolation between the equilibrium lattice parameters of the pure elements. In addition, the Cr-Cr and Cr-vacancy interaction energies up to second nearest neighbour were fitted, as well as the Cr-vacancy migration energy in Fe, using DFT reference values as guides [12]. All the mentioned properties were fitted using appropriate weights to obtain reasonable values. In addition to the expansion coefficients of the s-embedding functions and the mixed pair potential, there remains one degree of freedom that expresses the relative weight between the d-densities of Fe and Cr, ρ_{Fe}/ρ_{Cr}. By manually changing this fraction and consequently solving the quadratic programming problem, we fitted the excess vibrational entropy, computed in the harmonic approximation [31], to a value as close as possible to the experimental one, without losing the above properties and without stabilizing unphysical intermetallic compounds. Finally, the potential was manually adjusted in the small distance region to reproduce the DFT obtained binding energy of the mixed ⟨110⟩ Fe-Cr dumbbell.

The resulting parameters obtained from this procedure are presented in Appendix B, while some numerical issues associated with the functional form of the s-embedding terms are discussed in Appendix C. In what follows, we validate the potential against experiments and DFT data, and compare with the OLS and CAR potentials.

5. Validation of the Potential

5.1. Pure Elements

From the EAM type potentials available in the literature to describe pure Fe that are capable of reproducing the ⟨110⟩ self-interstitial configuration as the most stable, we considered those from Refs. [36], [27] and [45], finally selecting "potential 2" developed by Mendelev *et al.* [36] (henceforth M03), that has been widely used and tested. In [46] it has been demonstrated that existing *Mendelev-type* potentials ([36] and [27]) succeed best in reproducing the properties of iron that are of interest for radiation damage studies. However, of all, M03 is the only one for which a clear proof of being able to consistently describe screw dislocation glide exists [47].

Among the potentials for Cr , we considered those from Refs. [48] and [20]. The latter, henceforth O05, was used in combination with the Fe potential by Ackland *et al.* to produce the OLS and CAR potentials. The O05 potential, however, suffers a drawback regarding the ½ ⟨111⟩ screw-dislocation core, which has a three-fold symmetry, while a compact core is predicted by DFT [49]. For this purpose we fitted a new EAM type Cr potential, which is compared to the former in the following.

The basic properties of our potential are summarized and compared to O05 and DFT data in Table 1. In this table, $B=(C_{11}+2C_{12})/3$ is the bulk modulus, $C'=(C_{11}-C_{12})/2$ is the tetragonal shear and C_{44} is the shear modulus [41]. Clearly, the experimental elastic properties are well reproduced by both potentials. Note, however, that at zero Kelvin Cr is anti-ferromagnetic and has a negative Cauchy pressure [50], which cannot be reproduced within a standard central force framework [51-53]. Above its Néel temperature (~470 K), however, Cr

is paramagnetic with a positive Cauchy pressure [54]. Since we are interested in the alloy's properties at reactor temperatures (>600 K), our potential was fitted to the elastic constants of paramagnetic Cr, linearly extrapolated down to zero Kelvin (the values given in Table 1, see e.g. [48]). Furthermore, our potential also closely fits a_0, E_f^V, E_{coh} and E_m^V, obtaining improved values for the latter two. The relative stability between the different self interstitial configurations is not equally well reproduced as by O05, but the important features given by DFT are reproduced, i.e., the ⟨110⟩ and ⟨111⟩ configurations are almost degenerate and more stable than the ⟨100⟩ configuration. Finally, our potential is closer to DFT data regarding the bcc vs. fcc phase energy difference, thus providing enhanced stability of the bcc phase at high temperature. In summary, from the values presented in Table 1 we can conclude that the basic properties of Cr are equally well reproduced by both potentials.

Table 1 – Summary of the basic properties of both Cr potentials.

	Experiment or DFT	This Work	O05
a_0 (Å)	2.878 [a] / 2.834 [b]	2.866	2.878
B (GPa)	208 [c]	215	208
C' (GPa)	152 [c]	155	152
C_{44} (GPa)	105 [c]	108	105
E_{coh} (eV)	4.10	4.10	3.84
E_f^V (eV)	2.0 ± 0.2 [d] / 2.59 [b]	2.52	2.56
E_m^V (eV)	0.95 [e]	0.94	0.99
$E_{coh}^{fcc} - E_{coh}^{bcc}$ (eV)	-0.4 [f]	-0.16	-0.03
$E_f^{<110>} - E_f^{<111>}$ (eV)	-0.02 [b]	-0.07	-0.02
$E_f^{<110>} - E_f^{<100>}$ (eV)	-1.12 [b]	-0.58	-1.23

[a] Experiment, Ref. [55]
[b] DFT, Ref [20]
[c] Experiment, Ref. [54]
[d] Experiment, Ref. [56]
[e] Experiment, Ref. [57]
[f] Experiment, Ref. [58]

In Figure 1 the (110) ⟨111⟩ gamma surface cut calculated from our Cr potential and the Fe M03 potential are compared with their respective DFT values [49]. The figure shows that the DFT maximum for Fe is about half the one for Cr; a trend that is also reproduced by both potentials, even though they underestimate DFT by ~30 %.

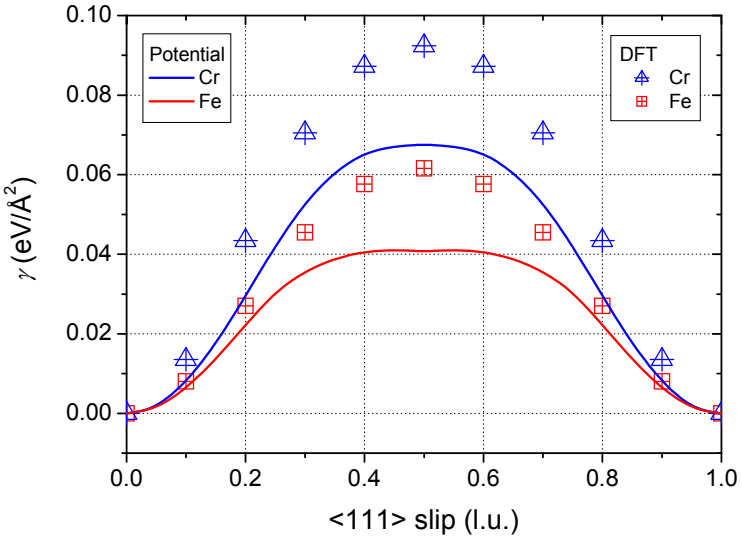

Figure 1 – Comparison between DFT [49] and the potentials of the (110) ⟨111⟩ gamma surface cut for Fe and Cr.

In Figure 2, the differential displacement maps for the screw dislocation core in Cr for our potential and O05 are compared, both obtained by static relaxations. Clearly, the latter shows a three-fold symmetry, while for the former the core structure is compact, as predicted by DFT. Worth of remarking is that on-going research (Terentyev et al. submitted) suggests a compact core provides a more consistent physical picture for the interaction between screw dislocations and Cr precipitates in the Fe matrix.

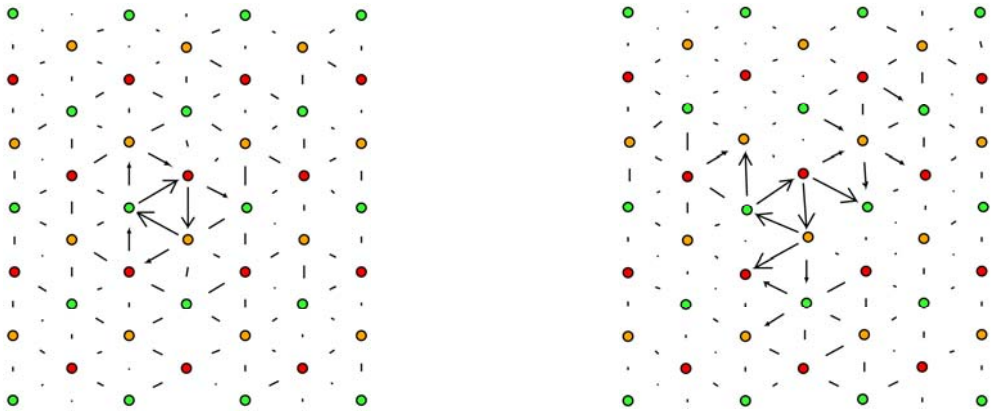

Figure 2 – Comparison of the screw component of differential displacement maps for both our potential (left) and the O05 potential (right).

5.2. Thermodynamic Properties of the Alloy

Here we discuss statically calculated thermodynamic properties and the phase diagram. The mixing enthalpy is tackled first, which is of relevance for disordered alloys. In such alloys there is no tendency for long-range order (i.e. in the absence of stable intermetallic compounds) and they are generally appropriate to describe the high temperature limit of the alloy. Next the formation energy of various intermetallic compounds is considered; in

particular low (negative) formation energies are relevant since they can introduce long and short-range order in the alloy, which generally govern the phase diagram at low temperature. Following this, we turn to the excess vibrational entropy, which, above the Debye temperature, can significantly influence the stability range of the phases. Finally the phase diagram is presented and discussed.

5.2.1. Mixing Enthalpy of Disordered Alloys

In Figure 3 the mixing enthalpy calculated with the three potentials is compared to DFT data [8, 12, 28]. Although different DFT techniques give different values for the mixing enthalpy, the DFT curves show the same behaviour, i.e., a change of sign in the mixing enthalpy, being negative below ~5 at.% Cr and positive above.

Both 2BM potentials were fitted to DFT data [12, 28] obtained from special quasi-random structures (SQSs) [59] while CAR was fitted to DFT data [8] obtained from a coherent potential approximation (CPA) [60]. The mixing enthalpy curves from our potential and CAR reproduce the DFT mixing enthalpy very well, both qualitatively and quantitatively. Below ~25 at.% Cr this is also true for OLS; the complete curve, however, takes a symmetric shape, in contrast to the asymmetric DFT shape. As a consequence, the mixing enthalpy takes negative values at the Cr-rich side too, leading to short-range order and high Fe solubility in the Cr-rich phase. These observations contradict DFT data and are experimentally unobserved.

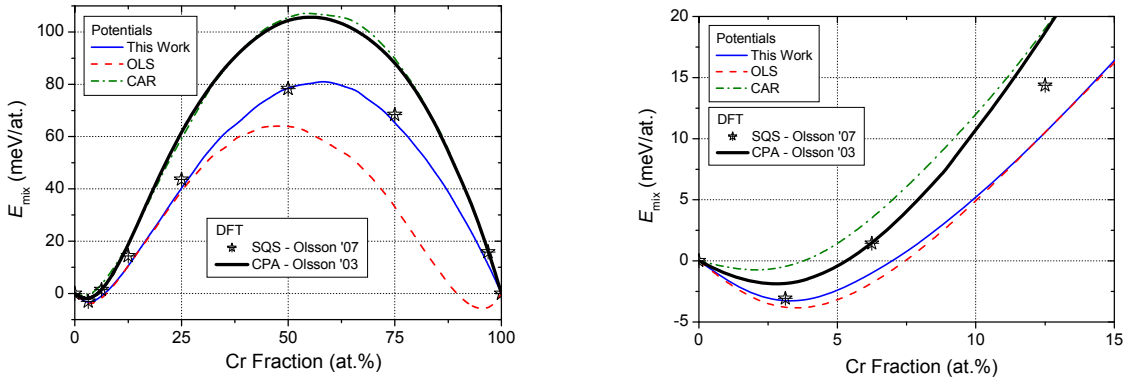

Figure 3 – Comparison of the mixing enthalpies obtained from the potentials with DFT data [8, 12, 28].

5.2.2. Formation Energy of Intermetallic Compounds

In Figure 4 the formation energy of 57 intermetallic compounds (as described in [11, 61]) calculated by the three potentials and DFT are compared. Below 10 at.% Cr DFT predicts stable intermetallic compounds, consistent with the negative mixing enthalpy for the disordered alloy. Above 10 at.% Cr, the formation energy of the intermetallic compounds becomes positive and remains so throughout the composition range.

In the Fe-rich region (< 10 at.%), the most stable compounds predicted by DFT are also the most stable predicted by all three potentials (see Figure 4), with most importantly the lowest compound at 6.67 at.% Cr (see Appendix D for the structure). Among the three, both

2BM potentials also give good quantitative agreement in that concentration range. At higher Cr composition (> 10 at.%), OLS generally overstabilizes the compounds thereby even giving negative values at 50 and 93.33 at.% Cr (see Figure 4 and Appendix D for the structure). The latter is consistent with the low (compared to DFT) and negative mixing enthalpy of the disordered alloy at equimolar and Cr-rich compositions, respectively. Such negative values in turn may lead to unphysical configurations in the course of e.g. Monte Carlo simulations, and thus constitute a serious drawback of the potential. The other two potentials do not suffer from the latter problems, although ours still somewhat overstabilizes the compounds.

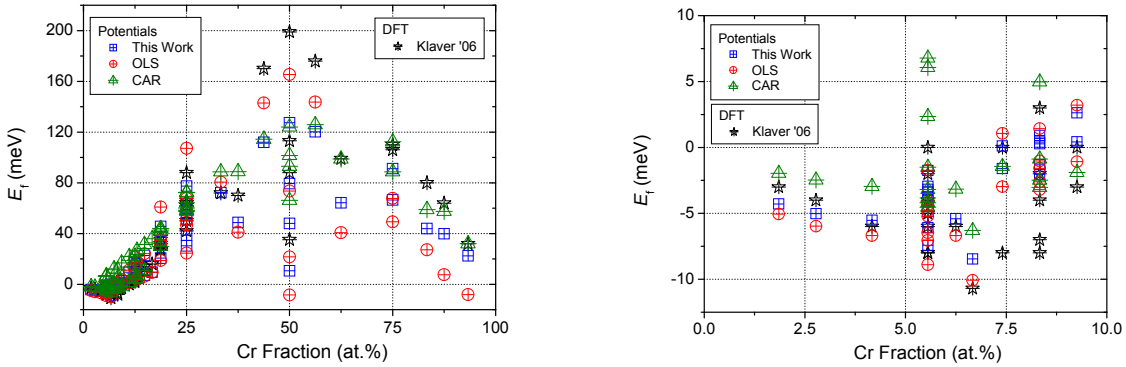

Figure 4 – Comparison of the formation energy obtained by the different potentials with the corresponding DFT values [11, 61] for various intermetallic compounds.

5.2.3. Excess Vibrational Entropy

In Figure 5 excess vibrational entropies for all three potentials are compared with experimental values for the ferro-magnetic phase [62, 63]. The experimental curves suggest a non-negligible contribution to the total excess entropy, amounting to 30-40% of the configurational entropy for the disordered alloy.

As shown in Figure 5, none of the potentials gives a close fit to the experimental values. From the three however, both 2BM agree best, with ours and OLS closest to the data from [62] and [63], respectively. In the former case the experimental data is underestimated by a factor of about 1.5; in the latter it is overestimated (below ~75 at.% Cr) by about the same factor. The CAR potential, on the other hand, underestimates S_{xc}^{vib} by about a factor 3 and gives negative contributions below ~12 at.% Cr, which contradicts experiments.

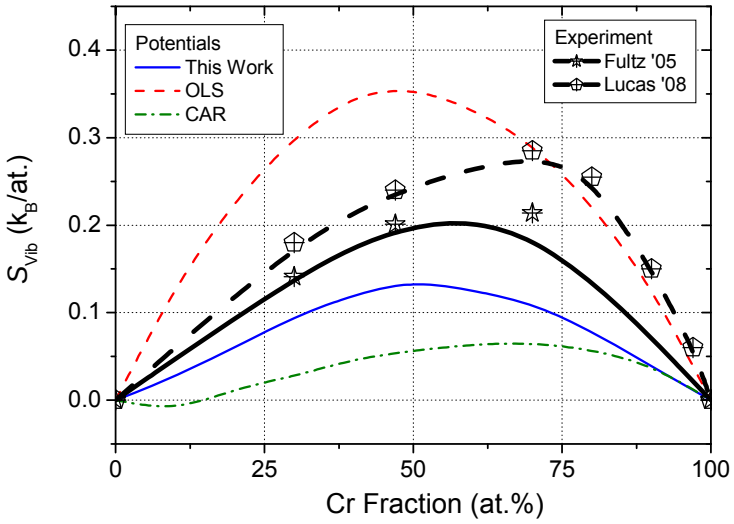

Figure 5 – Comparison of the excess vibrational entropy obtained from the different potentials with the experimental one from [62, 63].

5.2.4. Phase Diagram

In Figure 6 the phase diagrams based on all three potentials are compared to a recent proposal by the authors based on the CALPHAD methodology [64]. The calphad miscibility gap is calculated from an experimentally based [18, 65] Gibbs free energy parameterization. The phase boundaries for our potential and OLS are obtained from Monte Carlo simulations in the semi-grand canonical ensemble (transmutation ensemble) where vibrational entropy was included in an indirect way (see Section 3.2. and [28] for more details). The phase boundaries for CAR were obtained from free energy calculations using a thermodynamic integration technique (see [29] for more details). Thus in all cases vibrational and configurational entropy were accounted for in a direct or indirect way.

When focussed on the Fe-rich side, we observe large Cr solubility at low temperature, due to the negative heat of mixing. As shown in Figure 6, this behaviour is well reproduced by all potentials. At about 750K the Fe-rich solubility limit increases until full solubility is observed above the critical temperature ~900K within the CALPHAD calculation. The curve resulting from OLS follows this trend best, with a critical temperature ~1000K, closely followed by our potential, with a critical temperature ~1200K. The critical temperature resulting from CAR, on the other hand, lies above the melting temperature. Note that the difference in critical temperature between OLS and ours is mainly attributed to the difference in excess vibrational entropy.

On the Cr-rich side, little Fe solubility is observed at low temperature, which is well reproduced by both our potential and CAR. The OLS potential, on the other hand, predicts high Fe-solubility as an unphysical artefact of the negative heat of mixing at the Cr-rich side. We also note that for OLS a spurious phase corresponding to an intermetallic compound at 50at.% Cr may appear (see Section 5.2.2 and Appendix D). For simplicity, however, we have disregarded this phase as possible ground state in the calculation.

In summary, the essential high solubility of Cr at low temperature is well reproduced by all potentials, with OLS following the CALPHAD curve the best, closely followed by our

potential. For higher Cr content our potential and the CAR one seem to describe the CALPHAD curve more consistently.

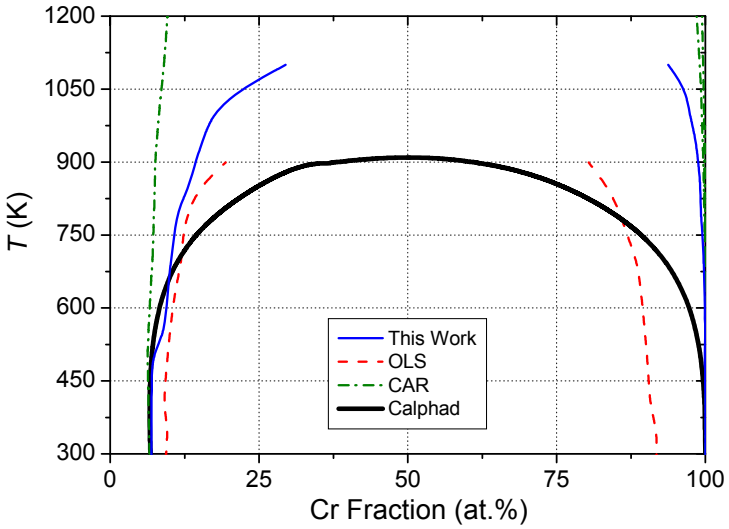

Figure 6 – Comparison of the phase diagrams resulting from the different potentials against a CALPHAD based calculation. The curves for the OLS potential, CAR potential and CALPHAD were taken from [28], [29] and [64], respectively.

5.3. Point-Defect Properties in the Alloy

In this section we discuss the energetic properties of point defect complexes that are essential to study radiation damage. Firstly, Cr-Cr interaction, Cr-vacancy interaction and vacancy migration barriers in bulk Fe are considered. The vacancy migration barriers combined with the Cr-Cr and Cr-vacancy interactions define the kinetic pathway followed under thermal annealing conditions. Next, interstitial defect interactions in the Fe matrix are tackled. In particular we consider the binding energy of Cr interstitial complexes and their migration in the Fe matrix. The combination of the latter and the substitutional point-defect properties control the kinetic pathway followed in thermal annealing conditions under irradiation.

5.3.1. Substitutional Defects

In Figure 7 the Cr-Cr and Cr-vacancy interaction energy in bulk Fe calculated from the three potential and DFT [12] is presented. The DFT data show Cr-Cr repulsion in bulk Fe that decreases fast with increasing distance. This behaviour is mainly responsible for the experimentally observed SRO and is acceptably well reproduced by all potentials. Both 2BM potentials, however, underestimate the difference in repulsion between first and second nearest neighbour Cr pairs; an effect that is well reproduced by CAR. Concerning the Cr-vacancy interaction, according to both DFT calculations [12] and experiments [66], it is essentially negligible. As shown in Figure 7, this feature is also qualitatively reproduced by all potentials, that predict slight repulsion between Cr and vacancy. Another important feature reproduced by all potentials is that the interaction energy between 1nn and 2nn Cr-vacancy

pairs increases. This is a necessity to obtain the correct order between forward and backward Cr-vacancy exchanges for several chemical environments in the Fe matrix, as discussed next.

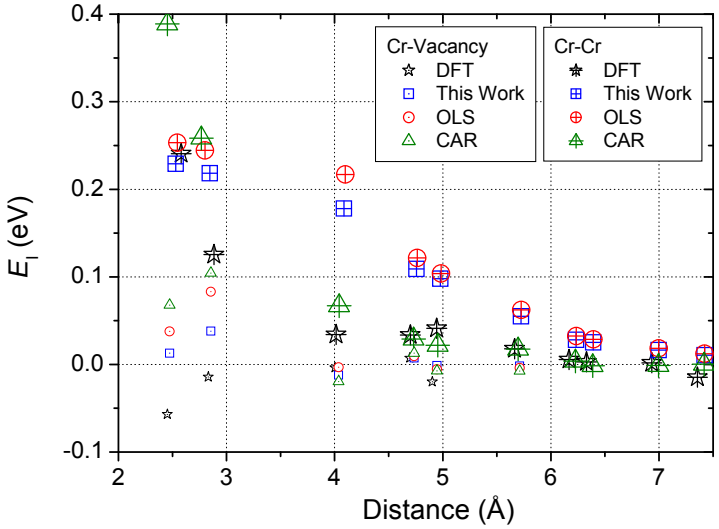

Figure 7 – Comparison between DFT and all three potentials of the interaction energy between Cr-Cr and Cr-vacancy pairs in bulk.

In Figure 8 the average (of forward and backward) vacancy migration barriers for different local Cr configurations calculated with the three potentials, are compared to the corresponding DFT values [67]. The DFT results show that the barriers are largest for both Cr and Fe exchanges when there are three Cr and three Fe atoms occupying the six nearest neighbour positions around the saddle-point. This effect is only reproduced by our potential, although OLS and CAR also give reasonable behaviour. Note, however, that in the case of the CAR potential, the value for Cr migration in bulk Fe is significantly overestimated. As a consequence, Cr migration barriers calculated with CAR are somewhat high compared to the corresponding DFT values. For the Fe jumps, on the other hand, the migration barriers are largely underestimated when locally enriched by three or more Cr atoms. A table summarizing both forward and backward jumps for all configurations on which Figure 8 is based is given in Appendix E.

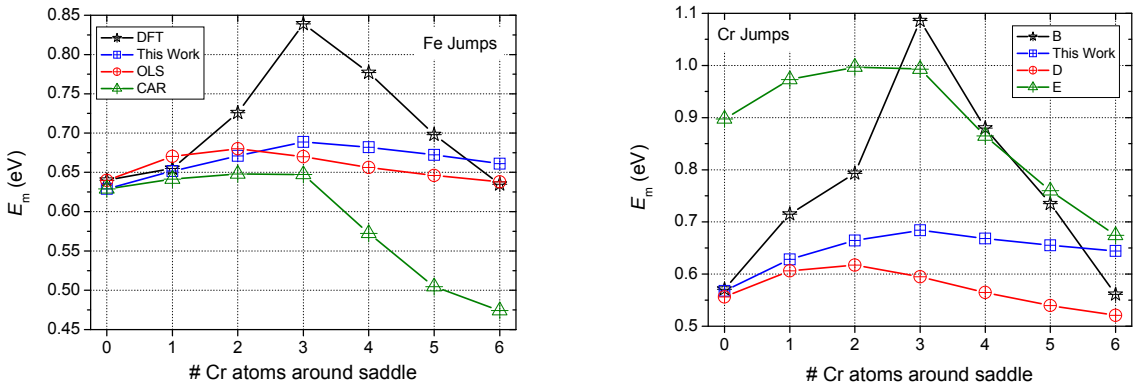

Figure 8 – Comparison between DFT and the three potentials of the average vacancy

migration barrier for different local Cr configurations (see Appendix E for details).

In summary, all three potentials reproduce Cr-Cr repulsion and negligible Cr-vacancy interaction, as suggested by DFT and experiments. Regarding vacancy migration barriers, both 2BM potentials succeed at best in reproducing the DFT data, especially the low barriers, which correspond to the most frequent transitions.

5.3.2. Interstitial Defects

In Figure 9 we show the formation energy of interstitial defects in bulk Fe and Cr, taking the ⟨110⟩ mixed dumbbell in bulk Fe as reference; values predicted by DFT [12] and the three potentials are compared. From the DFT data [12] it follows that the ⟨110⟩ mixed dumbbell configuration in bulk Fe is the lowest energy one. However, the inclusion of Cr in the defect diminishes the difference in formation energy between the ⟨111⟩ and ⟨110⟩ configurations. In pure Cr, on the other hand, all configurations are at least 0.7 eV above the corresponding configuration in pure Fe.

In the case of pure Fe, all potentials follow the DFT trend reasonably well, with a proper reproduction of the relative differences between the formation energies of the ⟨100⟩, ⟨110⟩ and ⟨111⟩ configurations being the most important feature. With the introduction of Cr, the data from our potential still captures the shape of the DFT curves reasonably well, while the data from OLS give almost degenerate values for all configurations. The CAR potential, on the other hand, fails to predict the ⟨110⟩ mixed dumbbell as the lowest energy configuration. Regarding the self-interstitial in pure Cr, all potentials follow the DFT trend reasonably well, the most important feature being the nearly degenerate formation energies of the ⟨110⟩ and ⟨111⟩ configurations. The large difference between interstitial configurations in bulk Fe and Cr predicted by DFT are well reproduced by the OLS and CAR potentials and less by ours. However, the difference between configurations in bulk Cr and the corresponding mixed configuration in bulk Fe amounts to at least 0.5 eV. This value is higher and, for the mixed ⟨110⟩ dumbbell at least, double the height of the corresponding Cr interstitial migration energies, as shown below. Therefore, an interstitial Cr atom is not expected to transfer into a Cr precipitate, in agreement with DFT [68].

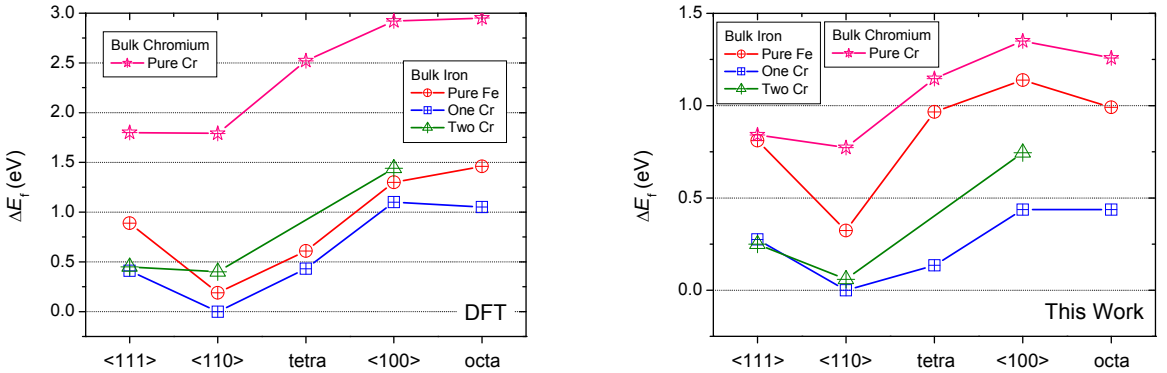

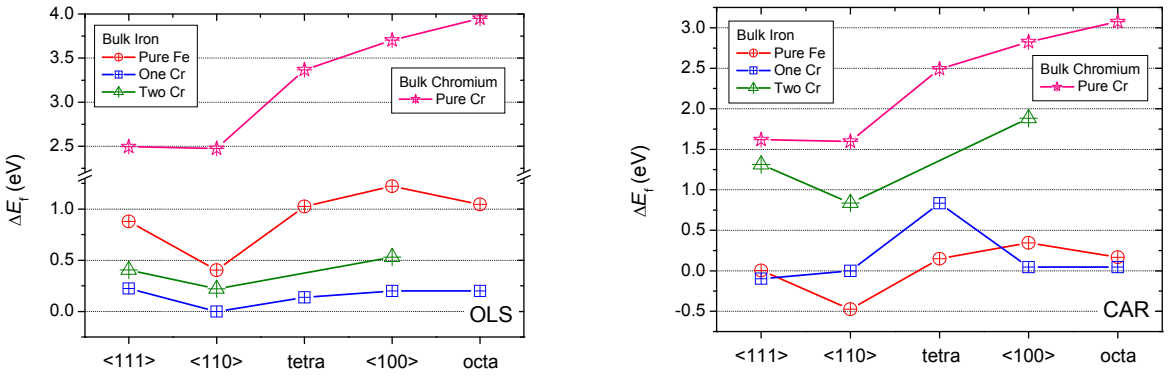

Figure 9 – Formation energies of different interstitial configurations in bulk Fe and Cr, calculated using DFT and the three different potentials.

Next, we compare the binding energy of Cr interstitials in bulk Fe obtained from the three potentials with the DFT values. Such a comparison is presented in Figure 10 (see Appendix F for the corresponding configurations). As expected from the above results, the CAR potential shows poor agreement with the DFT data. Given that both 2BM potentials were only fitted to the binding energy of the mixed ⟨110⟩ dumbbell, they show reasonable agreement with DFT. In particular, our potential is the only one that correctly reproduces the sign for all reported binding energies.

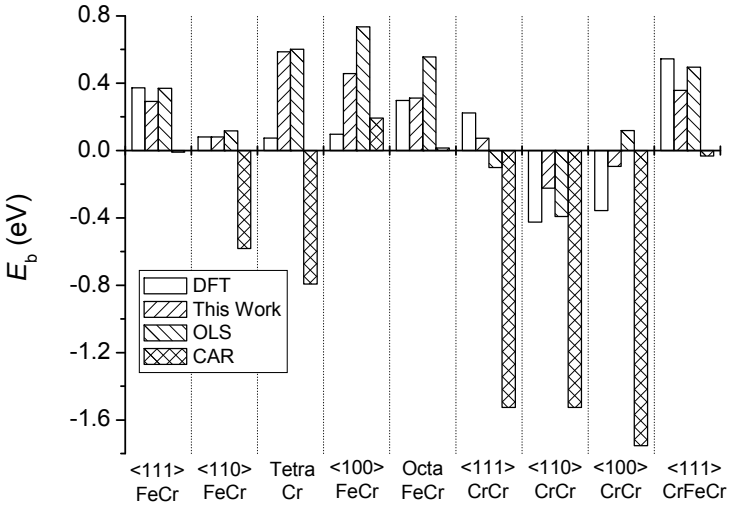

Figure 10 – Comparison between DFT and the three potentials of the binding energy of Cr interstitial configurations.

In Appendix F tables reporting formation and binding energies for interstitial configurations containing up to two Cr atoms can be found. As explained in Section 3.1, we can define an effective interaction energy E_I(CrCr) from such configurations. The results from DFT [12] and the three potentials are compared in Figure 11. We observe that the DFT values are smaller compared to the Cr-Cr interaction in substitutional positions (see Figure 7) and become even slightly attractive for certain configurations. The latter effect, though small, is essentially attributed to magnetic effects reducing the Cr-Cr repulsion under compression

[12]. As shown in Figure 11, none of the potentials or for that matter any EAM-type potential can reproduce this magnetic effect. Instead, the Cr-Cr repulsion follows the trend given in Figure 7, except for two points around 3.5 Å for both 2BM potentials. These points correspond to Cr configurations under strong compression (see Appendix F). Due to distortions following this compression, Equation (3) is no longer and therefore those points should be disregarded.

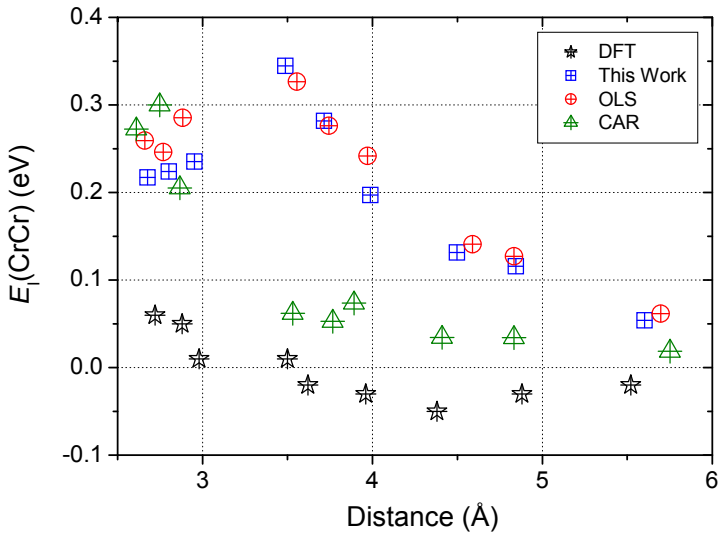

Figure 11 – Interaction energy between Cr-Cr pairs in the presence of an interstitial defect.

In Table 2 we compare energy barriers for different migration modes calculated with DFT and the 2BM potentials. Since CAR fails to reproduce the mixed ⟨110⟩ dumbbell as the most stable interstitial configuration it is disregarded for the present discussion. Based on the DFT results [69], the easiest migration mode in bulk Fe is Johnson's jump (configuration 2 of Table 2) for both Fe and Cr as migrating atom. 3-D migration of Cr via movement of a mixed ⟨110⟩ Fe-Cr dumbbell is therefore expected. The energy barriers for translation jumps involving Fe or Cr atoms (configurations 1 and 4) or on-site rotation (configuration 3), on the other hand, are fairly higher.

Regarding the migration barrier of a Fe-Fe ⟨110⟩ dumbbell, both 2BM potentials (and also CAR) show good qualitative agreement with the DFT data, predicting Johnson's jump to be the easiest migration mode. For the interstitial migration of Cr, on the other hand, for both 2BM potentials agreement with DFT is rather poor except for Johnson's jump. Besides Johnson's jump, two migration modes that are largely underestimated by the 2BM potentials become important, namely, the second nearest neighbour translation (configuration 5) and on-site rotation (configuration 4). Given that the on-site rotation barrier is only 0.02 and 0.01 eV higher than the barrier for Johnson's jump, the combination of second nearest neighbour translation with on-site rotation may offer an additional 3-D migration mechanism. The latter migration mechanism, however, is an artefact of the potentials and not supported by DFT data. Finally, we note a large discrepancy with Ref. [25] regarding the on-site rotation of the mixed ⟨110⟩ dumbbell. This and other discrepancies are probably due to the improper treatment of the s-embedding functions (as explained in Appendix C).

Table 2 – Interstitial migration barriers for different jumps in bulk Fe. In the figure black atoms are Fe and the grey atom is the migrating one (Fe or Cr).

Configuration		DFT	This Work	OLS
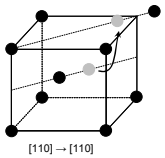 [110] → [110]	E_m^{Fe}	0.78	0.48	0.47
	E_m^{Cr}	0.42	0.35	0.32
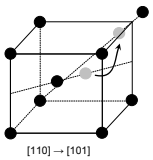 [110] → [101]	E_m^{Fe}	0.34	0.34	0.33
	E_m^{Cr}	0.23	0.24	0.21
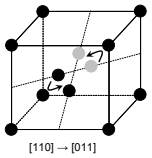 [110] → [011]	E_m^{Fe}	0.56	0.43	0.41
	E_m^{Cr}	0.36	0.26	0.22
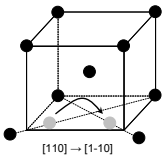 [110] → [1-10]	E_m^{Fe}	0.50	0.55	0.55
	E_m^{Cr}	0.43	0.23	0.18

In summary, both 2BM potentials reproduce the DFT interstitial formation and binding energies reasonably well. In particular our potential, which is the only one providing a correct sign for the reported binding energies. The CAR potential, on the other hand, fails to correctly describe the interstitial interactions. Both 2BM potentials predict an additional interstitial migration mechanism, in contrast to DFT, which is considered to be a serious shortcoming of the potentials.

6. Concluding Remarks

Here we discuss the advantages and disadvantages of the different potentials and their probable implications for atomistic simulations. A summary of the main properties discussed in this report is given in Table 3.

Table 3 – Schematic summary of the performance of the different potentials compared to DFT data and experiments.

Potential	Thermodynamics			Point-Defects			Dislocations
	Disordered Alloy	Intermetallic Compounds	Vibrational Entropy	Substitutional	Interstitial	Migration	
Here	Consistent	Consistent	Underestimated	Consistent	Consistent	Consistent	Consistent
2BM	Inconsistent	Inconsistent	Overestimated	Consistent	Consistent	Consistent	Inconsistent
CDM	Consistent	Consistent	Inconsistent	Consistent	Inconsistent	Inconsistent	Inconsistent

Based on the phase diagram, all potentials are capable of reproducing short-range order and α' precipitation. Our potential, however, seems the best compromise for thermodynamic modelling; it gives an asymmetric mixing enthalpy and does not stabilize unobserved intermetallic compounds, as opposed to OLS, and it provides (though underestimated) a significant amount of excess vibrational entropy, as opposed to CAR.

Based on the description of substitutional defect interactions and phase diagram, both the OLS and our potential *a priori* seem the best choice to simulate thermal annealing in Fe-Cr alloys. Besides a proper reproduction of the thermodynamic limit, a reasonable reproduction of vacancy migration barriers, Cr-Cr and Cr-V interactions assure that the correct kinetic path is followed using the correct mechanisms. All potentials provide a reasonable description of the Cr-Cr and Cr-vacancy interactions, but only the 2BM potentials provide reasonable values for vacancy migration barriers, with ours being the most consistent among the two.

Based on the description of interstitial and substitutional defect interactions and the phase diagram, both 2BM potential a priori seem the best choice to simulate thermal annealing of Fe-Cr alloys under irradiation. Besides a proper description of thermal annealing, a correct stabilization of interstitial complexes and their migration barriers are needed to assure that the correct micro-structure is obtained following the appropriate kinetic path under irradiation. Both 2BM potentials provide reasonable interstitial stabilities (ours in particular), but may provide a second migration mechanism that is unsupported by DFT. The latter is considered a shortcoming. The CAR potential, on the other hand, poorly predicts all interstitial properties.

Based on the description of the ½ ⟨111⟩ screw dislocation core structure (in bulk Fe and Cr) and its stable glide in the (110) plane in bulk Fe, our potential *a priori* seems the most suitable choice for the simulation of precipitate-screw dislocation interaction. From the three potentials, ours is the only one reproducing the compact ½ ⟨111⟩ screw dislocation core structure in bulk Cr and its Fe part has been proven to provide stable glide in the (110) plane.

In summary, we have shown that the newly developed Fe-Cr potential reached the goal of removing the main shortcomings of previously existing ones, while conserving their good properties. It should be noted, however, that it is not stiffened to the screened Coulomb interaction and is therefore not suitable to simulate collision cascades in its present form.

Acknowledgements

The authors thank Drs. P. Olsson, C. Domain, T.P.C. Klaver, D. Nguyen-Manh and M.Yu. Lavrentiev for fruitful discussions and their help in preparation of this report. This research has received partial funding from the European Atomic Energy Community's 7th Framework Programme (FP7/2007-2011), under grant agreement number 212175 (GetMat project). It also contributes to the European Fusion Technology programme (EFDA). The work was partially sponsored by the belgo-argentine MINCYT-FWO bilateral cooperation agreement, Project FW/07/EXII/002. RCP acknowledges support from CONICET-PICT 5062.

Appendix A: Chromium Potential

In this appendix we give the optimized parameters for the pure Cr potential. The parameterization for the density function φ is already given in Section 4.1. The spline coefficients for the pair interaction, V_{CrCr}, are given in Table A.1. As mentioned in Section 4.1, due to the fitting algorithm, the embedding function F is only available in tabulated form. As an indication, we provide twenty values of the potential functions in Table A.2. By applying an interpolation scheme between the tabulated points the reader can reproduce the potential functions and use them for approximate calculations. For more accurate calculations, like those reported in this report, the potential functions were tabulated up to 5000 points. Such tables are available on request.

Table A.1 – Spline coefficients to parameterize V_{CrCr} according to Equation (13).

r_k (Å)	a_k (eV/Å^3)
4.112494835E+00	-6.079639840E-02
3.738631668E+00	-8.216224618E-01
3.364768501E+00	2.424000178E+00
2.990905335E+00	-1.275324968E+00
2.617042168E+00	7.942650649E-01

Table A.2 – Tabulation of the Cr potential functions for approximate calculations.

r (Å)	$V_{CrCr}(r)$ (eV)	r (Å)	$\varphi(r)$	ρ	$F(\rho)$ (eV)
0.5000	14.0403	0.5000	17.5647	0.0000	-0.0004
0.6905	10.8094	0.6905	8.6776	0.1579	-1.1960
0.8811	8.0938	0.8811	4.6400	0.3158	-1.3247
1.0716	5.8496	1.0716	2.6025	0.4737	-1.4043
1.2621	4.0328	1.2621	1.5071	0.6316	-1.4346
1.4526	2.5993	1.4526	0.8929	0.7895	-1.4158
1.6432	1.5053	1.6432	0.5380	0.9474	-1.3477
1.8337	0.7065	1.8337	0.3284	1.1053	-1.2304
2.0242	0.1592	2.0242	0.2024	1.2632	-1.0640
2.2147	-0.1809	2.2147	0.1257	1.4211	-0.8483
2.4053	-0.3576	2.4053	0.0784	1.5789	-0.5834
2.5958	-0.4149	2.5958	0.0490	1.7368	-0.2693
2.7863	-0.3932	2.7863	0.0304	1.8947	0.0939
2.9768	-0.3108	2.9768	0.0185	2.0526	0.5064
3.1674	-0.1859	3.1674	0.0108	2.2105	0.9681
3.3579	-0.0715	3.3579	0.0059	2.3684	1.4790
3.5484	-0.0166	3.5484	0.0029	2.5263	2.0391
3.7389	-0.0032	3.7389	0.0011	2.6842	2.6484
3.9295	-0.0004	3.9295	0.0002	2.8421	3.3069
4.1200	0.0000	4.1200	0.0000	3.0000	4.0146

Appendix B: Iron-Chromium Potential

In this appendix we report the necessary parameters to construct the Fe-Cr potential. The s-density function φ^s was given in Section 4.2. The parameters defining the s-embedding functions F^s (see Equation (20)) and mixed pair potential V_{FeCr} (see Equation (13)) are summarized in Table B.1 and Table B.2, respectively.

Table B.1 – Expansion coefficients to parameterize F^s according to Equation (20).

	F^s_{Fe}	F^s_{Cr}
A_1	-0.217009784	-0.977557632E-02
A_2	0.388002579	0.374570104

Table B.2 – Spline coefficients to parameterize V_{FeCr} according to Equation (13).

r_k (Å)	a_k (eV/Å^3)
4.5	0.0748992889
4.11666667	0.01081841
3.73333333	-0.0322279809
3.35	-0.414828704
2.96666667	-0.0683226765
2.58333333	-2.55634481
2.2	5.57581564
2.33	16.22
2.15	-100

The potentials used to describe the pure species, Fe and Cr, are given in the work of Mendelev *et al.* [36] and Appendix A, respectively. As mentioned in Section 4.2, all pure potentials must be transformed to the effective potential gauge to be compatible with the cross potential derived here. The effective potential functions of the pure elements are obtained through the transformation $\hat{T}$,

$$\hat{T}\begin{cases} V^{\text{eff}}(r) = V(r) - 2C\varphi(r) \\ \varphi^{\text{eff}}(r) = S\varphi(r) \\ F^{\text{eff}}(\rho) = F(\rho/S) + C/S\rho \end{cases}, \tag{B.1}$$

where C and S are constants given in Table B.3. For approximate calculations a tabulation containing ~50 points is given in Tables B.4, B.5 and B.6. For precise calculations as the ones reported here, tabulations containing up to 5000 points are available on-line: http://www.ctcms.nist.gov/potentials/ or upon request to the authors. Note that a tabulation of the s-embedding functions is missing from Tables B.4, B.5 and B.6. As explained in Appendix C, due to the singular slope in the origin of the s-embedding functions, care should be exercised if used in tabular form.

Table B.3 – Transformation parameters for the pure potentials.

Element	*C*	*S*
Fe	0.116093429	0.0380008812
Cr	-0.0228765475	0.632643294

Table B.4 – Tabulation of the Fe potential functions for approximate calculations.

r (Å)	$V_{FeFe}(r)$ (eV)	r (Å)	$\varphi_{Fe}(r)$	ρ	$F_{Fe}(\rho)$ (eV)
1.000E+00	1.096E+02	1.000E+00	1.800E+00	0.000E+00	0.000E+00
1.088E+00	7.494E+01	1.065E+00	1.603E+00	8.163E-02	-1.218E+00
1.176E+00	5.014E+01	1.131E+00	1.422E+00	1.633E-01	-1.581E+00
1.263E+00	3.290E+01	1.196E+00	1.257E+00	2.449E-01	-1.805E+00
1.351E+00	2.123E+01	1.261E+00	1.107E+00	3.265E-01	-1.960E+00
1.439E+00	1.349E+01	1.327E+00	9.712E-01	4.082E-01	-2.071E+00
1.527E+00	8.455E+00	1.392E+00	8.489E-01	4.898E-01	-2.153E+00
1.614E+00	5.238E+00	1.457E+00	7.394E-01	5.714E-01	-2.212E+00
1.702E+00	3.213E+00	1.522E+00	6.418E-01	6.531E-01	-2.255E+00
1.790E+00	1.957E+00	1.588E+00	5.553E-01	7.347E-01	-2.285E+00
1.878E+00	1.187E+00	1.653E+00	4.793E-01	8.163E-01	-2.304E+00
1.965E+00	7.207E-01	1.718E+00	4.129E-01	8.980E-01	-2.315E+00
2.053E+00	4.199E-01	1.784E+00	3.554E-01	9.796E-01	-2.320E+00
2.141E+00	1.639E-01	1.849E+00	3.060E-01	1.061E+00	-2.318E+00
2.229E+00	-1.930E-02	1.914E+00	2.639E-01	1.143E+00	-2.313E+00
2.316E+00	-1.246E-01	1.980E+00	2.283E-01	1.224E+00	-2.303E+00
2.404E+00	-1.908E-01	2.045E+00	1.985E-01	1.306E+00	-2.290E+00
2.492E+00	-2.305E-01	2.110E+00	1.738E-01	1.388E+00	-2.275E+00
2.580E+00	-2.474E-01	2.176E+00	1.532E-01	1.469E+00	-2.258E+00
2.667E+00	-2.545E-01	2.241E+00	1.362E-01	1.551E+00	-2.240E+00
2.755E+00	-2.542E-01	2.306E+00	1.218E-01	1.633E+00	-2.220E+00
2.843E+00	-2.453E-01	2.371E+00	1.093E-01	1.714E+00	-2.200E+00
2.931E+00	-2.280E-01	2.437E+00	9.807E-02	1.796E+00	-2.178E+00
3.018E+00	-2.007E-01	2.502E+00	8.760E-02	1.878E+00	-2.157E+00
3.106E+00	-1.643E-01	2.567E+00	7.791E-02	1.959E+00	-2.136E+00
3.194E+00	-1.254E-01	2.633E+00	6.895E-02	2.041E+00	-2.114E+00
3.282E+00	-9.120E-02	2.698E+00	6.070E-02	2.122E+00	-2.093E+00
3.369E+00	-6.799E-02	2.763E+00	5.314E-02	2.204E+00	-2.073E+00
3.457E+00	-5.540E-02	2.829E+00	4.623E-02	2.286E+00	-2.053E+00
3.545E+00	-4.994E-02	2.894E+00	3.994E-02	2.367E+00	-2.034E+00
3.633E+00	-4.812E-02	2.959E+00	3.425E-02	2.449E+00	-2.016E+00
3.720E+00	-4.645E-02	3.024E+00	2.913E-02	2.531E+00	-1.999E+00
3.808E+00	-4.270E-02	3.090E+00	2.454E-02	2.612E+00	-1.983E+00
3.896E+00	-3.725E-02	3.155E+00	2.046E-02	2.694E+00	-1.968E+00
3.984E+00	-3.082E-02	3.220E+00	1.686E-02	2.776E+00	-1.955E+00
4.071E+00	-2.409E-02	3.286E+00	1.371E-02	2.857E+00	-1.943E+00
4.159E+00	-1.777E-02	3.351E+00	1.097E-02	2.939E+00	-1.932E+00
4.247E+00	-1.253E-02	3.416E+00	8.631E-03	3.020E+00	-1.923E+00
4.335E+00	-8.587E-03	3.482E+00	6.648E-03	3.102E+00	-1.916E+00
4.422E+00	-5.744E-03	3.547E+00	4.995E-03	3.184E+00	-1.911E+00
4.510E+00	-3.781E-03	3.612E+00	3.641E-03	3.265E+00	-1.907E+00
4.598E+00	-2.482E-03	3.678E+00	2.557E-03	3.347E+00	-1.905E+00
4.686E+00	-1.630E-03	3.743E+00	1.713E-03	3.429E+00	-1.905E+00
4.773E+00	-1.026E-03	3.808E+00	1.079E-03	3.510E+00	-1.907E+00
4.861E+00	-5.938E-04	3.873E+00	6.244E-04	3.592E+00	-1.910E+00
4.949E+00	-3.040E-04	3.939E+00	3.197E-04	3.673E+00	-1.916E+00
5.037E+00	-1.283E-04	4.004E+00	1.349E-04	3.755E+00	-1.924E+00
5.124E+00	-3.800E-05	4.069E+00	3.996E-05	3.837E+00	-1.934E+00
5.212E+00	-4.751E-06	4.135E+00	4.995E-06	3.918E+00	-1.946E+00
5.300E+00	0.000E+00	4.200E+00	0.000E+00	4.000E+00	-1.960E+00

Table B.5 – Tabulation of the Cr potential functions for approximate calculations.

r (Å)	$V_{CrCr}(r)$ (eV)	r (Å)	$\varphi_{Cr}(r)$	ρ	$F_{Cr}(\rho)$ (eV)
1.000E+00	6.867E+00	1.000E+00	3.134E+00	0.000E+00	-4.353E-04
1.064E+00	6.121E+00	1.064E+00	2.593E+00	8.163E-02	-1.107E+00
1.127E+00	5.431E+00	1.127E+00	2.153E+00	1.633E-01	-1.211E+00
1.191E+00	4.793E+00	1.191E+00	1.793E+00	2.449E-01	-1.287E+00
1.255E+00	4.204E+00	1.255E+00	1.498E+00	3.265E-01	-1.349E+00
1.318E+00	3.662E+00	1.318E+00	1.254E+00	4.082E-01	-1.397E+00
1.382E+00	3.165E+00	1.382E+00	1.053E+00	4.898E-01	-1.431E+00
1.446E+00	2.709E+00	1.446E+00	8.854E-01	5.714E-01	-1.452E+00
1.509E+00	2.294E+00	1.509E+00	7.461E-01	6.531E-01	-1.458E+00
1.573E+00	1.917E+00	1.573E+00	6.299E-01	7.347E-01	-1.451E+00
1.637E+00	1.576E+00	1.637E+00	5.325E-01	8.163E-01	-1.429E+00
1.700E+00	1.269E+00	1.700E+00	4.509E-01	8.980E-01	-1.394E+00
1.764E+00	9.945E-01	1.764E+00	3.823E-01	9.796E-01	-1.345E+00
1.828E+00	7.509E-01	1.828E+00	3.245E-01	1.061E+00	-1.282E+00
1.891E+00	5.361E-01	1.891E+00	2.758E-01	1.143E+00	-1.205E+00
1.955E+00	3.484E-01	1.955E+00	2.346E-01	1.224E+00	-1.114E+00
2.019E+00	1.862E-01	2.019E+00	1.997E-01	1.306E+00	-1.010E+00
2.082E+00	4.757E-02	2.082E+00	1.702E-01	1.388E+00	-8.912E-01
2.146E+00	-6.902E-02	2.146E+00	1.451E-01	1.469E+00	-7.588E-01
2.210E+00	-1.653E-01	2.210E+00	1.238E-01	1.551E+00	-6.125E-01
2.273E+00	-2.431E-01	2.273E+00	1.057E-01	1.633E+00	-4.523E-01
2.337E+00	-3.038E-01	2.337E+00	9.028E-02	1.714E+00	-2.782E-01
2.401E+00	-3.494E-01	2.401E+00	7.713E-02	1.796E+00	-9.030E-02
2.464E+00	-3.813E-01	2.464E+00	6.592E-02	1.878E+00	1.115E-01
2.528E+00	-4.014E-01	2.528E+00	5.634E-02	1.959E+00	3.272E-01
2.592E+00	-4.112E-01	2.592E+00	4.815E-02	2.041E+00	5.568E-01
2.656E+00	-4.123E-01	2.656E+00	4.112E-02	2.122E+00	8.003E-01
2.719E+00	-4.058E-01	2.719E+00	3.507E-02	2.204E+00	1.058E+00
2.783E+00	-3.920E-01	2.783E+00	2.986E-02	2.286E+00	1.329E+00
2.847E+00	-3.713E-01	2.847E+00	2.537E-02	2.367E+00	1.614E+00
2.910E+00	-3.442E-01	2.910E+00	2.149E-02	2.449E+00	1.913E+00
2.974E+00	-3.111E-01	2.974E+00	1.813E-02	2.531E+00	2.226E+00
3.038E+00	-2.726E-01	3.038E+00	1.524E-02	2.612E+00	2.553E+00
3.101E+00	-2.304E-01	3.101E+00	1.274E-02	2.694E+00	2.893E+00
3.165E+00	-1.868E-01	3.165E+00	1.058E-02	2.776E+00	3.248E+00
3.229E+00	-1.443E-01	3.229E+00	8.725E-03	2.857E+00	3.616E+00
3.292E+00	-1.052E-01	3.292E+00	7.131E-03	2.939E+00	3.999E+00
3.356E+00	-7.197E-02	3.356E+00	5.768E-03	3.020E+00	4.395E+00
3.420E+00	-4.657E-02	3.420E+00	4.606E-03	3.102E+00	4.805E+00
3.483E+00	-2.857E-02	3.483E+00	3.622E-03	3.184E+00	5.229E+00
3.547E+00	-1.658E-02	3.547E+00	2.794E-03	3.265E+00	5.667E+00
3.611E+00	-9.257E-03	3.611E+00	2.104E-03	3.347E+00	6.118E+00
3.674E+00	-5.224E-03	3.674E+00	1.536E-03	3.429E+00	6.584E+00
3.738E+00	-3.116E-03	3.738E+00	1.076E-03	3.510E+00	7.064E+00
3.802E+00	-1.775E-03	3.802E+00	7.120E-04	3.592E+00	7.557E+00
3.865E+00	-8.869E-04	3.865E+00	4.330E-04	3.673E+00	8.064E+00
3.929E+00	-3.591E-04	3.929E+00	2.298E-04	3.755E+00	8.585E+00
3.993E+00	-9.781E-05	3.993E+00	9.450E-05	3.837E+00	9.113E+00
4.056E+00	-9.324E-06	4.056E+00	2.004E-05	3.918E+00	9.640E+00
4.120E+00	0.000E+00	4.120E+00	0.000E+00	4.000E+00	1.017E+01

Table B.6 – Tabulation of the FeCr potential functions for approximate calculations.

r (Å)	$V_{FeCr}(r)$ (eV)	r (Å)	$\varphi^{s}_{FeCr}(r)$
1.000E+00	1.175E+02	1.000E+00	6.851E-01
1.071E+00	9.661E+01	1.088E+00	7.318E-01
1.143E+00	7.839E+01	1.176E+00	7.516E-01
1.214E+00	6.262E+01	1.263E+00	7.465E-01
1.286E+00	4.913E+01	1.351E+00	7.202E-01
1.357E+00	3.773E+01	1.439E+00	6.775E-01
1.429E+00	2.825E+01	1.527E+00	6.232E-01
1.500E+00	2.051E+01	1.614E+00	5.619E-01
1.571E+00	1.434E+01	1.702E+00	4.978E-01
1.643E+00	9.549E+00	1.790E+00	4.340E-01
1.714E+00	5.971E+00	1.878E+00	3.730E-01
1.786E+00	3.423E+00	1.965E+00	3.163E-01
1.857E+00	1.730E+00	2.053E+00	2.651E-01
1.929E+00	7.129E-01	2.141E+00	2.197E-01
2.000E+00	1.947E-01	2.229E+00	1.803E-01
2.071E+00	-2.223E-03	2.316E+00	1.466E-01
2.143E+00	-5.540E-02	2.404E+00	1.181E-01
2.214E+00	-1.158E-01	2.492E+00	9.446E-02
2.286E+00	-1.942E-01	2.580E+00	7.497E-02
2.357E+00	-2.609E-01	2.667E+00	5.909E-02
2.429E+00	-3.015E-01	2.755E+00	4.627E-02
2.500E+00	-3.213E-01	2.843E+00	3.601E-02
2.571E+00	-3.266E-01	2.931E+00	2.787E-02
2.643E+00	-3.236E-01	3.018E+00	2.145E-02
2.714E+00	-3.146E-01	3.106E+00	1.642E-02
2.786E+00	-3.005E-01	3.194E+00	1.252E-02
2.857E+00	-2.823E-01	3.282E+00	9.497E-03
2.929E+00	-2.609E-01	3.369E+00	7.175E-03
3.000E+00	-2.374E-01	3.457E+00	5.398E-03
3.071E+00	-2.124E-01	3.545E+00	4.046E-03
3.143E+00	-1.869E-01	3.633E+00	3.021E-03
3.214E+00	-1.616E-01	3.720E+00	2.248E-03
3.286E+00	-1.373E-01	3.808E+00	1.667E-03
3.357E+00	-1.148E-01	3.896E+00	1.232E-03
3.429E+00	-9.474E-02	3.984E+00	9.083E-04
3.500E+00	-7.703E-02	4.071E+00	6.675E-04
3.571E+00	-6.159E-02	4.159E+00	4.892E-04
3.643E+00	-4.829E-02	4.247E+00	3.575E-04
3.714E+00	-3.704E-02	4.335E+00	2.606E-04
3.786E+00	-2.769E-02	4.422E+00	1.895E-04
3.857E+00	-2.009E-02	4.510E+00	1.375E-04
3.929E+00	-1.405E-02	4.598E+00	9.953E-05
4.000E+00	-9.380E-03	4.686E+00	7.189E-05
4.071E+00	-5.897E-03	4.773E+00	5.181E-05
4.143E+00	-3.412E-03	4.861E+00	3.727E-05
4.214E+00	-1.747E-03	4.949E+00	2.675E-05
4.286E+00	-7.370E-04	5.037E+00	1.917E-05
4.357E+00	-2.184E-04	5.124E+00	1.321E-05
4.429E+00	-2.730E-05	5.212E+00	3.959E-06
4.500E+00	0.000E+00	5.300E+00	0.000E+00

Appendix C: Some Numerical Issues

This appendix concerns numerical issues associated to the functional form for the s-embedding terms. As shown in Equation (20), we chose a typical second moment expression, characterized by a square root dependence of the density. Derived in its original framework [37], for the bulk of a material, this expression is never evaluated near zero density. However, given the specific conditions of the s-density functions for the application to the alloy (see Equation (17)), the s-density can reach values close to zero in a dilute alloys, meaning that the forces due to the s-embedding function become singular.

Frequently, potentials are tabulated on a grid of ~5000 points between the extreme values of the density (as a conservative estimate, we take 0 and 1, which are the extremes for our s-density on a perfect lattice). Such tables, in turn, are typically interpolated by cubic splines to obtain values in between grid points. A comparison of such an interpolation with the analytic expression is given in Figure C.1 for the Fe s-embedding function. Clearly, due to the cusp of the square root, there is a deviation of ~0.6 meV between the interpolated and analytic expression in the first interval, while starting from the second interval, the difference is negligible. If we now take bulk Fe with an isolated Cr atom, the Fe atoms in the 4nn and 5nn shells from the Cr atom take a value for the s-density in the first interval of the tabulation, as indicated by the arrows in Figure C.1. When computing the total energy of the latter system, we find a discrepancy of ~20 meV due to the spline interpolation of the s-embedding function.

We can thus conclude that a typical tabulation of the s-embedding function introduces a non-negligible systematic error of ~20 meV in the total energy per isolated Cr atom added to the Fe matrix. Therefore, special care must be taken to compute the energy and force contribution of the s-embedding terms and we recommend that the proper analytic expression is used to describe the s-embedding functions, rather than tabulations.

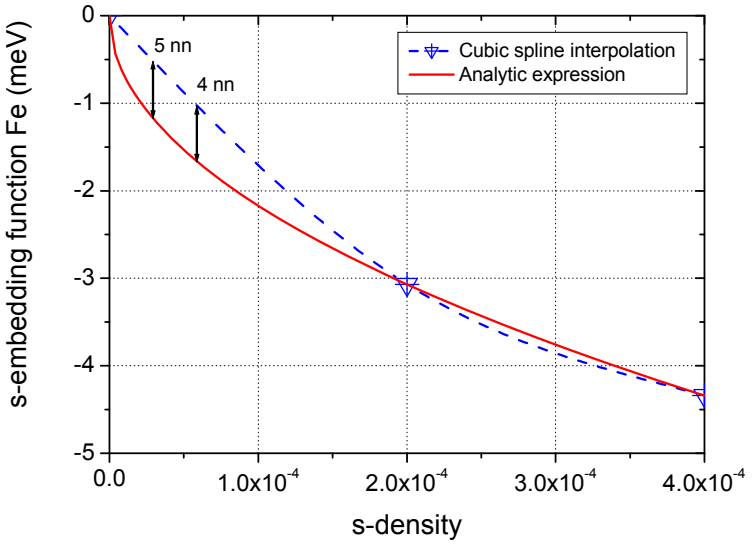

Figure C.1 – Comparison between the analytic expression for the Fe s-embedding function with a cubic spline expansion on a typical grid.

Appendix D: Intermetallic Compounds

In this appendix we give a description of the structure of the intermetallic compounds with lowest formation energy. The first compound is the one at 6.67 at.%, which is predicted to be the most stable at the Fe-rich side by DFT and the potentials. At the Cr-rich side, the same compound is also wrongly stabilized by the OLS potential. Starting from a bcc lattice, the unit cell is orthogonal with axes oriented along the $[210]$, $[\bar{1}20]$ and $[001]$ directions with dimensions $\sqrt{5}\,a_0 \times \sqrt{5}\,a_0 \times 3a_0$. The unit cell contains 30 atoms, of which 2 solute separated by 7nn distance ($\sqrt{19}/2\,a_0$) along $[133]$.

The other compound is the one at 50 at.%, which the OLS potential wrongly stabilizes. Starting from a bcc lattice, the compound consists of an alternate (110) planes stacking of the form … FeFeCrCrFeFe …

Appendix E: Vacancy Migration Barriers

In this appendix we provide the migration barriers for Fe-Vacancy and Cr-Vacancy exchange for different local chemical environments. The latter are build by adding Cr atoms around the six nearest neighbour positions around the migration saddle point. A comparison between DFT and the potentials for such configurations is given in Table E.1.

Table E.1 – The vacancy migration barrier for different local Cr configurations, with the first and second value denoting the forward and backward jump, respectively. In the figure black circles are Fe, white ones are Cr, in grey is the migrating atom, and the square represents the vacancy.

Configuration		DFT	This Work	OLS	CAR
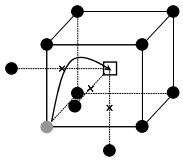	E_m^{Cr}	0.57 / 0.57	0.57 / 0.57	0.56 / 0.56	0.90 / 0.90
	E_m^{Fe}	0.64 / 0.64	0.63 / 0.63	0.64 / 0.64	0.63 / 0.63
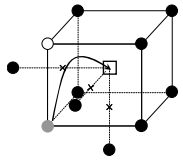	E_m^{Cr}	0.72 / 0.54	0.63 / 0.57	0.61 / 0.53	0.97 / 0.87
	E_m^{Fe}	0.66 / 0.60	0.65 / 0.63	0.67 / 0.63	0.64 / 0.62
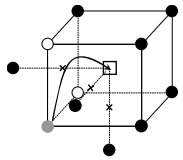	E_m^{Cr}	0.79 / 0.52	0.66 / 0.58	0.62 / 0.51	1.00 / 0.85
	E_m^{Fe}	0.73 / 0.57	0.67 / 0.63	0.68 / 0.61	0.65 / 0.61
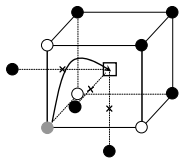	E_m^{Cr}	1.09 / 0.69	0.68 / 0.58	0.59 / 0.49	0.99 / 0.82
	E_m^{Fe}	0.84 / 0.55	0.69 / 0.63	0.67 / 0.60	0.65 / 0.59
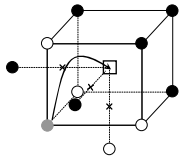	E_m^{Cr}	0.88 / 0.55	0.67 / 0.61	0.56 / 0.51	0.86 / 0.77
	E_m^{Fe}	0.78 / 0.58	0.68 / 0.64	0.66 / 0.62	0.57 / 0.55
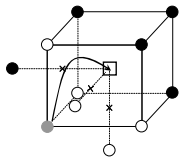	E_m^{Cr}	0.74 / 0.56	0.66 / 0.62	0.54 / 0.52	0.76 / 0.72
	E_m^{Fe}	0.70 / 0.61	0.67 / 0.65	0.65 / 0.64	0.50 / 0.50
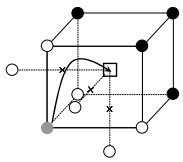	E_m^{Cr}	0.56 / 0.56	0.64 / 0.64	0.52 / 0.52	0.67 / 0.67
	E_m^{Fe}	0.64 / 0.64	0.66 / 0.66	0.64 / 0.64	0.47 / 0.47

Appendix F: Binding Energy of Interstitial Configurations

In this appendix we provide the binding and formation energy for various Fe-Cr interstitial complexes in the Fe matrix. In Tables F.1 and F.2 a comparison between DFT and the three potential of the binding and formation energy is given for interstitial complexes containing one Cr and two Cr atoms, respectively. In the latter tables, all possibilities for Cr atoms up to first nearest neighbour around the interstitial position are enumerated.

Table F.1 – Binding and formation energy of different interstitial configurations in the Fe matrix containing a single Cr atom (in white).

Configuration	DFT	This Work	OLS	CAR
1 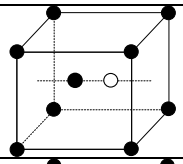	$E_b = 0.10$ $E_f = 4.93$	$E_b = 0.46$ $E_f = 3.64$	$E_b = 0.73$ $E_f = 3.33$	$E_b = 0.19$ $E_f = 4.05$
2 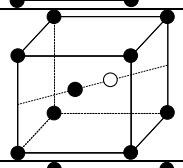	$E_b = 0.08$ $E_f = 3.83$	$E_b = 0.08$ $E_f = 3.20$	$E_b = 0.12$ $E_f = 3.13$	$E_b = -0.58$ $E_f = 4.00$
3 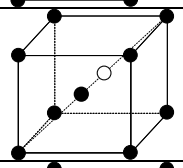	$E_b = 0.37$ $E_f = 4.24$	$E_b = 0.29$ $E_f = 3.48$	$E_b = 0.37$ $E_f = 3.35$	$E_b = -0.01$ $E_f = 3.91$
4 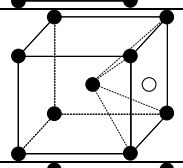	$E_b = 0.30$ $E_f = 4.88$	$E_b = 0.31$ $E_f = 3.64$	$E_b = 0.56$ $E_f = 3.33$	$E_b = 0.02$ $E_f = 4.05$
5 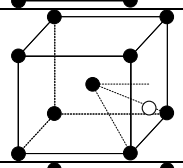	$E_b = 0.07$ $E_f = 4.26$	$E_b = 0.59$ $E_f = 3.34$	$E_b = 0.60$ $E_f = 3.26$	$E_b = -0.79$ $E_f = 4.84$
6 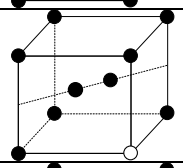	$E_b = -0.07$ $E_f = 3.98$	$E_b = 0.09$ $E_f = 3.19$	$E_b = 0.12$ $E_f = 3.12$	$E_b = 0.11$ $E_f = 3.31$
7 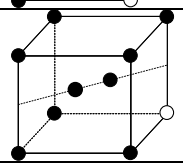	$E_b = 0.05$ $E_f = 3.86$	$E_b = 0.02$ $E_f = 3.27$	$E_b = 0.05$ $E_f = 3.19$	$E_b = -0.27$ $E_f = 3.69$

Table F.2 – Binding and formation energy of different interstitial configurations in the Fe matrix containing two Cr atoms.

Configuration	DFT	This Work	OLS	CAR
1 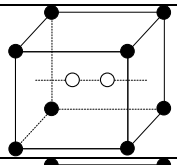	E_b = -0.36 E_f = 5.27	E_b = -0.09 E_f = 3.95	E_b = 0.12 E_f = 3.66	E_b = -1.75 E_f = 5.89
2 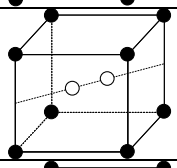	E_b = -0.43 E_f = 4.23	E_b = -0.22 E_f = 3.26	E_b = -0.39 E_f = 3.35	E_b = -1.53 E_f = 4.84
3 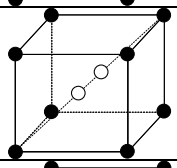	E_b = 0.22 E_f = 4.28	E_b = 0.07 E_f = 3.45	E_b = -0.10 E_f = 3.53	E_b = -1.53 E_f = 5.32
4 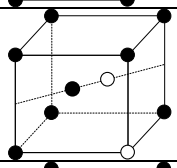	E_b = -0.02 E_f = 3.82	E_b = -0.04 E_f = 3.08	E_b = -0.02 E_f = 2.98	E_b = -0.74 E_f = 4.06
5 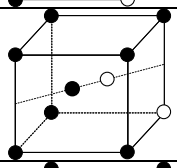	E_b = -0.21 E_f = 4.01	E_b = -0.20 E_f = 3.24	E_b = -0.25 E_f = 3.21	E_b = -1.23 E_f = 4.55
6 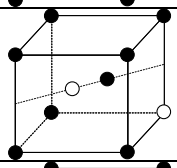	E_b = 0.15 E_f = 3.65	E_b = -0.19 E_f = 3.23	E_b = -0.11 E_f = 3.06	E_b = -0.90 E_f = 4.21
7 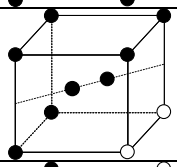	E_b = -0.04 E_f = 3.84	E_b = -0.13 E_f = 3.17	E_b = -0.11 E_f = 3.06	E_b = -0.36 E_f = 3.68
8 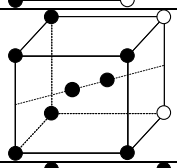	E_b = 0.09 E_f = 3.71	E_b = -0.31 E_f = 3.35	E_b = -0.22 E_f = 3.18	E_b = -0.59 E_f = 3.91
9 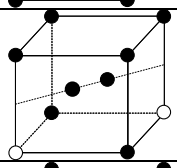	E_b = 0.15 E_f = 3.65	E_b = -0.10 E_f = 3.14	E_b = -0.03 E_f = 2.99	E_b = -0.57 E_f = 3.88
10 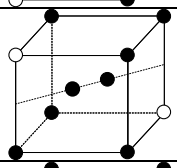	E_b = 0.12 E_f = 3.68	E_b = -0.02 E_f = 3.06	E_b = 0.04 E_f = 2.91	E_b = -0.55 E_f = 3.86
11 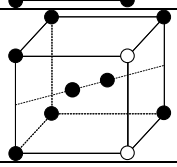	E_b = -0.20 E_f = 4.00	E_b = -0.04 E_f = 3.08	E_b = 0.00 E_f = 2.95	E_b = -0.08 E_f = 3.40

12	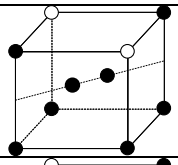	E_b = -0.12 E_f = 3.92	E_b = -0.01 E_f = 3.05	E_b = 0.01 E_f = 2.95	E_b = 0.14 E_f = 3.17
13	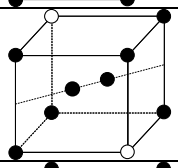	E_b = -0.12 E_f = 3.92	E_b = 0.07 E_f = 2.97	E_b = 0.12 E_f = 2.84	E_b = 0.18 E_f = 3.13
14	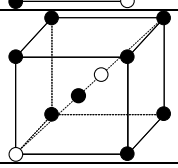	E_b = 0.54 E_f = 3.95	E_b = 0.36 E_f = 3.17	E_b = 0.50 E_f = 2.94	E_b = -0.03 E_f = 3.82

References

[1] E.A. Little and D.A. Stow, J. Nucl. Mater. 87 (1979) 25.
[2] E.A. Little and D.A. Stow, J. Metal Sci. 14 (1980) 89.
[3] S.I. Porollo, A.M. Dvoriashin, A.N. Vorobyev and Yu.V. Konobeev, J. Nucl. Mater. 256 (1998) 247.
[4] F.A. Garner, M.B. Toloczko and B.H. Sencer, J. Nucl. Mater. 276 (2000) 123.
[5] Yu.V. Konobeev, A.M. Dvoriashin, S.I. Porollo and F.A. Garner, J. Nucl. Mater. 355 (2006) 124.
[6] H. Kayano, A. Kimura, M. Narui, Y. Sasaki, Y. Suzuki and S. Ohta, J. Nucl. Mater. 155-157 (1988) 978.
[7] A. Kohyama, A. Hishinuma, D.S. Gelles, R.L. Klueh, W. Dietz and K. Ehrlich, J. Nucl. Mater. 233-237 (1996) 138.
[8] P. Olsson, I.A. Abrikosov, L. Vitos and J. Wallenius, J. Nucl. Mater. 321 (2003) 84.
[9] A.A. Mirzoev, M.M. Yalalov and D.A. Mirzaev, Phys. Met. Metall. 97 (2004) 336.
[10] P. Olsson, I.A. Abrikosov and J. Wallenius, Phys. Rev. B 73 (2006) 104416.
[11] T.P.C. Klaver, R. Drautz and M.W. Finnis, Phys. Rev. B 74 (2006) 094435.
[12] P. Olsson, C. Domain and J. Wallenius, Phys. Rev. B 75 (2007) 014110.
[13] D. Nguyen-Manh, M.Yu. Lavrentiev and S.L. Dudarev, J. Computer-Aided Mater. Des. 14 (2007) 159.
[14] P. Erhart, B. Sadigh and A. Caro, Appl. Phys. Lett. 92 (2008) 141904.
[15] I. Mirebeau, M. Hennion and G. Parette, Phys. Rev. Lett. 53 (1984) 687.
[16] N.P. Filippova, V.A. Shabashov and A.L. Nikolaev, Phys. Met. Metall. 90 (2000) 145.
[17] V.V. Sagaradze, I.I. Kositsyna, V.L. Arbuzov, V.A. Shabashov and Yu.I. Filippov, Phys. Met. Metall. 92 (2001) 89.
[18] J.-O. Andersson and B. Sundman, CALPHAD 11 (1987) 83.
[19] G. Bonny, D. Terenty and L. Malerba, Scr. Mater. 59 (2008) 1193.
[20] P. Olsson, J. Wallenius, C. Domain, K. Nordlund and L. Malerba, Phys. Rev. B 72 (2005) 214119.
[21] A. Caro, D.A. Crowson and M. Caro, Phys. Rev. Lett. 95 (2005) 75702.
[22] G. Bonny, R.C. Pasianot, L. Malerba, Philos. Mag. 89 (2009) 711.
[23] P. Olsson, J. Wallenius, C. Domain, K. Nordlund and L. Malerba, Phys. Rev. B 74 (2006) 1(E).
[24] D. Terentyev, P. Olsson, T.P.C. Klaver and L. Malerba, Comp. Mater. Sci. 43 (2008) 1183.
[25] D. Terentyev and N. Castin, J. Comput. Mater. Sci. 46 (2009) 1178.
[26] G. Bonny, D. Terentyev, L. Malerba and D. Van Neck, Phys. Rev. B 79 (2009) 104207.
[27] G.J. Ackland, M.I. Mendelev, D.J. Srlolovitz, S. Han and A.V. Barashev, J. Phys. Condens. Mat. 16 (2004) 1.
[28] G. Bonny, R.C. Pasianot, L. Malerba, A. Caro, P. Olsson and M.Yu. Lavrentiev, J. Nucl. Mater. 385 (2009) 268.
[29] G. Bonny, P. Erhart, A. Caro, R.C. Pasianot, L. Malerba and M. Caro, Modelling Simul. Mater. Sci. Eng. 17 (2009) 025006.
[30] H. Jonsson, G. Mills, and K. W. Jacobsen, in Nudged Elastic Band Method for Finding Minimum Energy Paths of Transitions, Classical and Quantum Dynamics in Condensed Phase Simulations, Eds. B. J. Berne, G. Ciccotti, and D. F. Coker (World Scientific, Singapore, 1998.
[31] A. van de Walle and G. Ceder, Rev. Mod. Phys. 74 (2002) 11.

[32] A. van de Walle and G. Ceder, Journal of Phase Equilibria 23 (2002) 348.
[33] A. van de Walle and M. Asta, Modelling Simul. Mater. Sci. Eng. 10 (2002) 521.
[34] G.D. Garbulsky and G. Ceder, Phys. Rev. B 49 (1994) 6327.
[35] M.S. Daw and M.I. Baskes, Phys. Rev. B 29 (1984) 6443.
[36] M.I. Mendelev, A. Han, D.J. Srolovitz, G.J. Ackland, D.Y. Sun and M. Asta, Phil. Mag. A 83 (2003) 3977.
[37] M.W. Finnis and J.E. Sinclair, Phil. Mag. A 50 (1984) 45.
[38] F. Ercolessi, M. Parrinello and E. Tosatti, Phil. Mag. A 58 (1988) 213.
[39] R.A. Johnson and D.J. Oh, J. Mater. Res. 4 (1989) 1195.
[40] J. Nocedal and S.J. Wright, *Numerical Optimization*, Springer-Verlag, New York, 2006, p. 449.
[41] C. Kittel, *Introduction to Solid State Physics*, John Wiley & Sons, New York, 1996 (chapter 3).
[42] M.S. Duesbery and V. Vitek, Acta Mater. 46 (1998) 1481.
[43] J.H. Rose, J.R. Smith, F. Guinea and J. Ferrante, Phys. Rev. B 29 (1984) 2963.
[44] G.J. Ackland and S.K. Reed, Phys. Rev. B 67 (2003) 174108.
[45] S.L. Dudarev and P.M. Derlet, J. Phys.: Condens. Matter 17 (2005) 7097 (2005).
[46] L. Malerba, M.C. Marinica, N. Anento, C. Björkas, H. Nguyen, C. Domain, F. Djurabekova, P. Olsson, K. Nordlund, A. Serra, D. Terentyev, F. Willaime and C.S. Becquart, J. Nucl. Mater. 406 (2010) 19.
[47] C. Domain and G. Monnet, Phys. Rev. Lett. 95 (2005) 215506.
[48] J. Wallenius, P. Olsson, C. Lagerstedt, N. Sandberg, R. Chalarova and V. Pontikis, Phys. Rev. B 69 (2004) 094103.
[49] C. Domain, private communication.
[50] H.J. van Rijn and H.L. Alberts, J. Phys. F 13 (1983) 1559.
[51] R. Pasianot, D. Farkas and E.J. Savino, Phys. Rev. B 43 (1991) 6952.
[52] O. Yifang, Z. Bangwei, L. Shuzhi and J. Zhanpeng, Z. Phys. B 101 (1996) 161.
[53] Z. Bangwei, O. Yifang, L. Shuzhi and J. Zhanpeng, Physica B 262 (1999) 218.
[54] K. Katahara, M. Nimalendran, M. Manghnani and E. Fischer, J. Phys. F: Met. Phys. 9 (1979) 2167.
[55] W. Pearson, *A Handbook of Lattice Spacings and Structures of Metals and Alloys*, Pergamon Press, New York, 1958.
[56] G. Loper, L. Smedskjaer, M. Chason, and R. Siegel, *Positron Annihilation*, Eds P. Jain et al., World Scientific, Singapore, 1985, p. 461.
[57] H. Schultz, Mater. Sci. Eng., A 141 (1991) 149.
[58] S. Cottenier, private communication, June (2009).
[59] A. Zunger, S.H. Wei, L.G. Ferreira and J.E. Bernard, Phys. Rev. Lett. 65 (1990) 353.
[60] B.L. Györffy, Phys. Rev. B 5 (1972) 2382.
[61] T.P.C. Klaver, G. Bonny, P. Olsson and D. Terentyev, Modelling Simul. Mater. Sci. Eng. 18 (2010) 075004.
[62] B. Fultz, L. Anthony, J.L. Robertson, R.M. Nicklow, S. Spooner and M. Mostoller, Phys. Rev. B 52 (1995) 3280.
[63] M.S. Lucas, M. Kresch, R. Stevens and B. Fultz, Phys. Rev. B 77 (2008) 184303.
[64] N. Saunders, A.P. Miodownik, CALPHAD Calculation of Phase Diagrams: A Comprehensive Guide, Pergamon, Kidlington, 1998.
[65] G. Bonny, D. Terentyev and L. Malerba, J. Phase Equil. Diffus. 31 (2010) 439.
[66] A. Möslang, H. Graf, G. Balzer, E. Recknagel, A. Weidinger, Th. Wichert and R.I. Grynszpan, Phys. Rev. B 27 (1983) 2674.
[67] D. Nguyen-Manh, M.Yu. Lavrentiev and S.L. Dudarev, C. R. Physique 9 (2008) 379.

[68] P. Olsson, J. Nucl. Mater. 386-388 (2009) 86.
[69] C.C. Fu, F. Willaime and P. Ordejon, Phys. Rev. Lett. 92 (2004) 175503.